TITLE PAGE

Heterozygosity for neurodevelopmental disorder-associated *TRIO* variants yields distinct deficits in behavior, neuronal development, and synaptic transmission in mice.

Yevheniia Ishchenko*[1], Amanda T. Jeng*[1,2], Shufang Feng[1,3], Timothy Nottoli[4], Cindy Manriquez-Rodriguez[5], Khanh K. Nguyen[5], Melissa G. Carrizales[1], Matthew J. Vitarelli[1], Ellen E. Corcoran[1], Charles A. Greer[2,6,7], Samuel A. Myers[5], Anthony J. Koleske[1,2,6]

1. Department of Molecular Biophysics and Biochemistry, Yale University, New Haven, CT, USA
2. Interdepartmental Neuroscience Program, Yale University, New Haven, CT, USA
3. Department of Gerontology, The Third Medical Center, Chinese PLA General Hospital, Beijing, China
4. Department of Comparative Medicine, Yale School of Medicine, New Haven, CT, USA
5. Laboratory for Immunochemical Circuits, La Jolla Institute for Immunology, La Jolla, CA, USA
6. Department of Neuroscience, Yale School of Medicine, New Haven, CT, USA
7. Department of Neurosurgery, Yale School of Medicine, New Haven, CT, USA

* These authors contributed equally to this work.

ABSTRACT

Genetic variants in *TRIO* are associated with neurodevelopmental disorders (NDDs) including schizophrenia (SCZ), autism spectrum disorder (ASD) and intellectual disability. TRIO uses its two guanine nucleotide exchange factor (GEF) domains to activate GTPases (GEF1: Rac1 and RhoG; GEF2: RhoA) that control neuronal development and connectivity. It remains unclear how discrete *TRIO* variants differentially impact these neurodevelopmental events. Here, we investigate how heterozygosity for NDD-associated *Trio* variants – *+/K1431M* (ASD), *+/K1918X* (SCZ), and *+/M2145T* (bipolar disorder, BPD) – impact mouse behavior, brain development, and synapse structure and function. Heterozygosity for different *Trio* variants impacts motor, social, and cognitive behaviors in distinct ways that align with clinical phenotypes in humans. *Trio* variants differentially impact head and brain size with corresponding changes in dendritic arbors of motor cortex layer 5 pyramidal neurons (M1 L5 PNs). Although neuronal structure was only modestly altered in the *Trio* variant heterozygotes, we observe significant changes in synaptic function and plasticity. We also identified distinct changes in glutamate synaptic release in *+/K1431M* and *+/M2145T* cortico-cortical synapses. The TRIO K1431M GEF1 domain has impaired ability to promote GTP exchange on Rac1, but *+/K1431M* mice exhibit increased Rac1 activity, associated with increased levels of the Rac1 GEF Tiam1. Acute Rac1 inhibition with NSC23766 rescued glutamate release deficits in *+/K1431M* variant cortex. Our work reveals that discrete NDD-associated *Trio* variants yield overlapping but distinct phenotypes in mice, demonstrates an essential role for Trio in presynaptic glutamate release, and underscores the importance of studying the impact of variant heterozygosity in vivo.

INTRODUCTION

Neurodevelopmental disorders (NDDs), including autism spectrum disorder (ASD), intellectual disability (ID), developmental delay (DD), schizophrenia (SCZ) and bipolar disorder (BPD), disrupt brain development and function. NDDs share considerable comorbidities and present with overlapping symptoms, including impairments in cognition, behavior, language, social and motor skills, emotions, and learning ability (1). In addition, the risk genes for NDDs overlap significantly, further suggesting shared mechanistic underpinnings and pathology for these disorders (2, 3).

TRIO encodes a large cytoskeletal regulatory protein with two guanine nucleotide exchange factor (GEF) domains for Rho family GTPases - GEF1 activates Rac1 and RhoG, while GEF2 activates RhoA (4-6). TRIO relays signals from cell surface receptors, acting on GTPases to coordinate cytoskeletal rearrangements critical for proper neurodevelopment (7-15). *Trio* knockout mice exhibit decreased survival, skeletal muscle defects, and severe defects in brain development (16-18). Selective ablation of *Trio* in either excitatory or inhibitory neurons alters their morphology, impairs synaptic signaling, and yields NDD-related behavioral defects (19, 20). Trio deficiency also leads to aberrations in long-term potentiation (LTP), as Trio-Rac1 signaling promotes AMPA receptor trafficking to increase synaptic strength (19, 21, 22).

Damaging *de novo* mutations and ultra-rare variants in *TRIO* are enriched in individuals with NDDs (23-30). Interestingly, nonsense variants spread throughout *TRIO* are enriched in individuals with SCZ (30, 31), whereas pathogenic missense *TRIO* variants in or surrounding the GEF1 domain are associated with ASD/ID (24, 28, 29). Variants in the Trio GEF1 domain that decrease Rac1 activity are associated with milder ID and microcephaly, whereas variants in the adjacent spectrin repeat 8 domain that increase Rac1 activity are associated with more severe ID and macrocephaly (25, 26, 32, 33). Rare missense variants in *TRIO* have also been observed in BPD, epilepsy, and other disorders, but studies to date are underpowered to establish a causal link with these disorders. How distinct heterozygous *TRIO* variants differentially impact mammalian brain development and lead to diverse phenotypes remains a fundamental and unresolved question.

We report here the comprehensive analysis of mice heterozygous for discrete *Trio* variants associated with different NDDs ASD-associated *+/K1431M* in the Trio GEF1 domain, SCZ-associated *+/K1918X,* leading to nonsense decay, and BPD-associated *+/M2145T* in Trio GEF2 domain. We show that distinct *Trio* NDD-associated variants differentially impair mouse behavior, brain development, and inhibitory and excitatory synaptic transmission. We show, for the first time, that *Trio* variants that impact GEF1 and GEF2 activity differentially impact

presynaptic neurotransmitter release and synaptic vesicle replenishment. While the Trio K1431M GEF1 domain is impaired in Rac1 activation, unexpectedly *+/K1431M* mice exhibit increased Rac1 activity, associated with increased levels of the Rac1 GEF Tiam1. Acute Rac1 inhibition with NSC23766 rescued glutamate release deficits in *+/K1431M* variant cortex. Together, our data show how discrete heterozygous *TRIO* variants that differentially impact Trio biochemical activities yield divergent effects on behavior, neurodevelopment, and synaptic transmission.

MATERIALS AND METHODS

Animal work

Animal work was compliant with federal guidelines and approved by the Yale Institutional Animal Care and Use Committee. Age-matched male and female mice were used for behavioral experiments; males were used for electrophysiological and neuroanatomical studies to reduce potential variation due to estrus cycle (34).

Generation of *Trio* mutant mice and mouse genotyping

Mice heterozygous for *Trio* variants *K1431M*, *K1918X*, or *M2145T* were generated via CRISPR/Cas-mediated genome editing and maintained on a C57Bl/6 background. Details on allele design and genotyping are included in Supp. Methods.

In vitro GEF Assays

The *K1431M* point mutant was generated via site-directed mutagenesis of human WT TRIO GEF1 using the following oligos: 5'-cagcgaataacgatgtatcagctcc-3' and 5'-ggagctgatacatcgttattcgctg-3'. Recombinant WT and *K1431M* human TRIO GEF1 and Rac1 were purified from bacteria as described (35). GEF activity was monitored by the decrease in fluorescent signal ($\lambda_{excitation}$ = 488 nm; $\lambda_{emission}$ = 535 nm) as GTP was exchanged for BODIPY-FL-GDP on Rac1 over 30 min, as described (33, 35).

Body weight, brain weight, and head width measurements

Ear-to-ear head width of P42 mice was measured with calipers in anesthetized mice. Brain weight was measured after removing the olfactory bulbs and brain stem.

Mouse brain lysates and cortical synaptosome preparation

Whole brain lysates from P0-P1 or P35-P42 mice, and cortical synaptosomes from P39-P42 mice, were prepared as previously described (19, 36, 37), with minor modifications (described in Supp. Methods). Protein concentrations were determined with BCA assay (Pierce).

Western blot and quantification

Brain lysates were separated on SDS-PAGE gels, blotted to nitrocellulose membranes, stained with Ponceau S, blocked in 5% nonfat milk in TBS-T, incubated with primary antibodies overnight at 4°C, then with conjugated secondary antibodies at RT for 1 h (see Supp. Table 1 for list of antibodies). Images captured by a ChemiDoc Imaging System (Bio-Rad) were quantified in ImageJ. Signal intensity was normalized to Ponceau S, then to the WT average.

G-LISA

GTP-bound active Rac1 and RhoA levels in were measured using G-LISA kits according to manufacturer's instructions (Cytoskeleton, Inc., BK128; Inc., BK124).

Behavioral tests

Behavioral tests were performed in mice 6-8 weeks of age (P42-P56), as previously described (19).

Animal perfusion and tissue processing

Mice were transcardially perfused with heparinized PBS followed by 4% paraformaldehyde (PFA) in phosphate buffered saline (PBS). Brains were postfixed in 4% PFA at 4°C for 24 h, then sliced coronally at 30 µm for Nissl stain and immunohistochemistry and 200 µm for dendritic arbor and spine analysis. For details on tissue processing, see Supp. Methods.

Electron microscopy

Electron microscopy of synapses in M1 layer 5 was performed as previously described (19) and synaptic features were quantified in ImageJ as previously described (38-41) from 5-18 fields of view (~50 μm^2) per mouse by a reviewer blinded to genotype.

Electrophysiological recordings

Acute slices were prepared from mice at P35-42 as previously described (19) with modifications noted here. Coronal slices of M1-M2 cortex were cut at 360 µm in ice-cold N-Methyl-D-glucamine-aCSF (NMDG-aCSF, in mM): 120 NMDG, 2.5 KCl, 7 $MgSO_4$, 1.25 NaH_2PO_4, 0.5 $CaCl_2$, 28 $NaHCO_3$, 13 glucose, 7 sucrose, saturated with 95% O2-5% O2 at 300-320 mOsmol/L, pH 7.4) on a vibratome (Leica) and recovered in normal ACSF at 32ºC for 30 min followed by 1 h recovery at RT. Recorded signals were acquired at 100kHz sampling rate and low pass filtered at 6 kHz. Cells were excluded if series resistance changed >20%.

AMPAR- and NMDAR- eEPSCs, miniature EPSCs (mEPSCs), Long term-potentiation (LTP) and were recorded and analyzed as previously described in (19). Gamma-aminobutyric acid receptor and glycine receptor miniature inhibitory postsynaptic currents (GABAR/GlyR-mIPSCs) were recorded at +15 mV.

Paired-pulse stimulation was applied and paired-pulse ratio (PPR) was calculated as described in (19). Calculations of the readily releasable pool (RRP) size, probability of release (Pr) and synaptic vesicles (SVs) depletion and RRP recovery (fractional) rate were made from

recordings of AMPAR-eEPSCs under high frequency stimulation (HFS, 40Hz; 15 pulses) for each neuron as previously described (42-44) (details see in **Supp. Methods**).

Rescue experiments were performed as described above with addition of 100 μM NSC23766 into the recording solution with 5 min incubation period to allow for efficient slice penetration. All train data were processed and analyzed using OriginLab 10 software.

Quantitative Proteomics

Tissue from P21 mouse cortex (4 per genotype) was processed for tandem mass tag (TMT) peptide labeling as previously described (19) with minor modifications. Desalted 16-plex TMT-labeled peptides were separated by HPLC, and proteome analysis was performed using an EASY-nLC 1200 UHPLC coupled to an Orbitrap Eclipse mass spectrometer (Thermo Fisher Scientific). MS2 spectra were searched using Spectrum Mill (Agilent) against the UniProt Mouse Database. Technical details are described in **Supp. Methods.**

Gene Set Enrichment Analysis

Mouse UniProtIDs for identified proteins were converted to human orthologs and ranked by signed $\log_{10}$(nominal p-value) (with sign indicating direction of fold-change from WT). GSEA 4.3.3 (45, 46) was used to run the GSEAPreranked tests against all gene sets in the Human MSigDB Collection C2 v2023.2. SynGO 1.2 (47) was used to identify synaptic ontologies for differentially expressed proteins with nominal p-value <0.05.

Data Analysis

Statistical analyses were performed using GraphPad Prism 10. Data in bar graphs are presented as mean ±SEM, with individual data points graphed when applicable. Sample size 'n' is annotated within the bars or in the figure legend for each group. Distributions were tested for normality and outliers were removed before proceeding with statistical tests. Specific details of statistical tests performed, adjusted with post-hoc Bonferroni test for multiple comparisons (MC) where appropriate, are included in the figure legends. Significance was defined by a p-value less than 0.05: ^{ns}p<0.1; *p<0.05; **p<0.01; ***p<0.001; ****p<0.0001.

RESULTS

Generation of *Trio* variant mice and impact on *Trio* isoforms

We used CRISPR/Cas9 technology to generate mice bearing heterozygous *Trio* rare variant alleles associated with ASD (*+/K1431M*) and SCZ (*+/K1918X*), and a *de novo* mutation found in an individual with BPD (*+/M2145T*) **(Fig. 1A,B)**. We chose these alleles for their discrete effects on TRIO levels or activity: K1431M impairs TRIO GEF1 activity in vitro up to 8-fold **(Supp. Fig. 1A,B)** (24), M2145T TRIO GEF2 has reduced ability to activate RhoA as a function of protein concentration in cells (24), and K1918X creates a premature stop codon between GEF1 and GEF2.

Mice heterozygous for these *Trio* alleles survived to adulthood. Mice homozygous for *Trio K1431M* and *M2145T* survived to adulthood, with genotypes from offspring of *+/K1431M* intercrosses observed in Mendelian ratios, but fewer than expected *M2145T* homozygotes obtained **(Supp. Fig. 1C)**. *K1918X* homozygote pups were not observed, as expected for a null allele (16, 18). We focused on heterozygotes, as most rare damaging *Trio* variants are heterozygous in humans. Heterozygosity for the *K1431M* and *M2145T* alleles did not alter the levels of the predominant Trio isoforms (Trio9S, 263 kDa; Trio9L, 277 kDa; Duet, 145 kDa; cerebellum-specific Trio8 217 kDa (48, 49)) in the brain at postnatal day 0 (P0) **(Fig. 1C-D)** or P42 **(Fig. 1A, Supp. Fig. 1D-L)**. Trio9 protein levels were reduced by ~50% in the brains of *+/K1918X* mice at P0 **(Fig. 1C-D)** and P42, and we did not detect residual truncated protein (expected 217 kDa), suggesting this mutation leads to nonsense-mediated decay **(Supp. Fig. 1D-L)**; levels of Trio8 and Duet were unaffected **(Supp. Fig. 1D-L)**.

Trio variant alleles differentially impact active Rho family GTPase levels.

Given the effects of these variants on TRIO GEF1/2 activities, we measured levels of active GTP-bound Rac1 and RhoA in brains of neonatal (P0) and adult (P42) *Trio* variant-bearing mice **(Fig. 1E-H)**. In concordance with the ~50% reduction in Trio levels in *+/K1918X* brains, Rac1 activity was decreased in P0 *+/K1918X* brains (91% of WT activity), with a trend toward decreased active RhoA levels (84% of WT, p=0.0865). By P42, *+/K1918X* brains did not differ from WT in Rac1 or RhoA activity.

As K1431M decreases TRIO GEF1 catalytic activity in vitro **(Supp. Fig. 1A,B)** (20, 24, 29), we anticipated Rac1 activity might be reduced in *+/K1431M* mice. Instead, active Rac1 levels were *increased* in *+/K1431M* whole brain lysates compared to WT controls at P0 (**(Fig. 1E)**,111% of WT) and even higher at P42 (**(Fig. 1G)**, 150% of WT). We also did not detect changes in active RhoA levels at the whole brain lysate level in *+/M2145T* mice at either age **(Fig. 1F,H)**.

Because Trio, Rac1, and RhoA are enriched at synapses (15, 22, 24, 50), we also measured their activities in synaptosomes **(Supp. Fig. 1M-P)**. Rac1 activity was significantly increased in *+/K1431M* crude synaptosomes from P42 cortex (112% of WT) **(Fig. 1I)**, consistent with measurements in whole brain lysates. Consistent with its reduced GEF2 activity, RhoA activity was decreased in *+/M2145T* synaptosomes compared to WT (73% of WT) **(Fig. 1J)**.

Distinct *Trio* variants differentially impact mouse behavior.

NDDs affect learning and memory, compulsivity, motor coordination, and social skills, hence we assessed these skills using a diverse array of established behavioral tests (19) in mice bearing *Trio* variants. *+/K1431M* and *+/K1918X* mice of both sexes fell from an accelerating rotarod with reduced latency and improved more slowly in this skill over repeated trials relative to WT littermates **(Fig. 1K, Supp. Fig. 1Q)**, while *+/M2145T* mice performed similarly to WT. No deficits in muscle strength were noted in any genotype using the Kondziela inverted screen test prior to rotarod testing, and no differences in locomotor or exploratory activity were seen in an open field test (data not shown). In a three-chamber social interaction test, *+/K1431M* mice of both sexes showed no preference for the stranger mouse over the object **(Fig. 1L, Supp. Fig. 1R)**. *+/M2145T* mice of both sexes and *+/K1918X* males exhibited preference for the stranger mouse, similar to WT. In a novel object recognition test, *+/K1918X* mice of both sexes and *+/M2145T* females failed to discriminate between the novel and familiar objects, while *+/K1431M* mice and *+/M2145T* males exhibited normal discrimination between novel and familiar objects similar to WT **(Fig. 1M, Supp. Fig. 1S)**. *+/K1918X* males exhibited significantly more compulsive nestlet shredding relative to WT, while *+/K1431M* males showed a trend toward increased nestlet shredding **(Fig. 1N)**.

Overall, behavioral phenotypes overlapped between *+/K1431M* and *+/K1918X* mice, though there were distinct differences in social interaction and memory tests. *+/M2145T* mice exhibited the fewest phenotypes in measured tasks. Together, these data indicate that these *Trio* alleles differentially impact behavior.

***Trio +/K1431M* and *+/K1918X* mice have smaller brains.**

TRIO variants that reduce TRIO GEF1 activity are associated with microcephaly (25, 26, 33), so we assessed head and brain size in *Trio* variant mice **(Fig. 2A-E, Supp. Fig. 2A-E)**. After adjusting for body weight, both the head width and brain weight **(Fig. 2D,E)** were reduced in adult *+/K1431M* mice relative to WT, consistent with the microcephaly seen in patients harboring *TRIO* GEF1-deficient alleles. Head width in *+/K1918X* mice was reduced, but in proportion to their body weight (head width-to-body weight ratios did not differ between

+/K1918X and WT mice, p>0.95). However, *+/K1918X* mice still displayed a reduced brain weight relative to WT, suggesting a disproportionate reduction in brain mass relative to their already smaller head size. Meanwhile, *+/M2145T* mice did not differ from WT in either head width or brain weight when adjusted for body weight.

***Trio* variant mice show limited changes in cortical organization.**

We examined whether the decreased brain weight and head size observed in *+/K1431M* and *+/K1918X* mice were associated with anatomical defects. Histological analyses did not reveal gross morphological defects (data not shown). We observed reductions in both total cross-sectional brain area and cortical thickness in *+/K1918X* brains **(Fig. 2F-H)**, consistent with their smaller head size and brain weight. Significant decreases in cortical layer 2/3 and layer 5 thickness were observed in *+/K1918X* brains; but these were in proportion to the relative decrease in cortical thickness as compared to WT **(Supp. Fig. 2F-H)**. No changes were observed in *+/M2145T* mice.

No differences in total cortical cell density or in layer-specific cell density were observed in *Trio* variant mice relative to WT, nor were numbers or proportions of cortical NeuN+ neuronal cells or PV+ inhibitory neurons altered relative to WT, although there were trends toward increased cell density in *+/K1918X* cortex and increased NeuN+ cell density in *+/M2145T* motor cortex **(Supp. Fig. 2M-Q)**. These data suggested that the reduced brain size *+/K1918X* mice resulted from a loss of neuropil.

***Trio* variant heterozygotes exhibit alterations in dendritic arbors and synaptic ultrastructure.**

Altered dendritic arbor morphology and dendritic spine abnormalities are hallmarks of NDDs (51-57). Excitatory neuron-specific ablation of one or both *Trio* alleles decreased dendritic arborization, increased spine density, and yielded smaller synapses in cortex area M1 Layer 5 pyramidal neurons (M1 L5 PNs) (19).

Sholl analysis of M1 L5 PNs revealed significant reductions in both basal and apical dendritic arbor complexity and dendritic field size in P42 *+/K1918X* neurons, an increase in proximal basal arbor complexity in *+/K1431M* neurons, and a slight decrease in distal apical arbor complexity in *+/M2145T* neurons relative to WT **(Fig. 2I-M)**. Path length analysis revealed that branch numbers were increased for lower order dendrites in *+/K1431M* neurons, while average branch lengths were decreased at higher order dendrites in *+/K1918X* neurons **(Supp. Fig. 3F-K)**. None of the *Trio* variant heterozygotes exhibited altered dendritic spine

density on M1 L5 pyramidal neurons compared to WT mice on either apical or basal arbors **(Supp. Fig. 3L,M**).

Electron microscopy of cortical area M1 L5 revealed that synapse density was significantly increased in *+/K1918X* mice compared to WT **(Fig. 3A,B)**, possibly due to a net reduction in neuropil resulting from smaller dendritic arbors. Within synapses, postsynaptic density (PSD) length was slightly decreased in *+/K1918X* and *+/M2145T* mice, but not in *+/K1431M* mice **(Fig. 3C)**. Cross-sectional presynaptic bouton area and spine head area were similar to WT in each *Trio* variant heterozygote **(Fig. 3D,E)**.

Synaptic vesicle (SV) distribution was significantly altered in *+/M2145T* mice relative to the other genotypes **(Fig. 3F,G)**. Within the total releasable pool 15-150 nm from the active zone (AZ), both docked SVs at 15nm comprising the readily-releasable pool (RRP) (40, 41) and tethered SVs at 50 nm were significantly increased in density in *+/M2145T* mice relative to the other genotypes **(Fig. 3F,G)**. SVs distribution at 200 nm from the AZ which contribute to the reserve pool were also significantly increased in *+/M2145T*, suggesting an overall SV pool size. No differences in synaptic vesicle distribution were noted in *+/K1431M* mice, while *+/K1918X* showed modestly increased SVs at 200 nm from AZ relative to WT.

Synaptic transmission and plasticity are differentially impaired by distinct *Trio* variants. Loss of Trio function or disruption of TRIO GEF1 activity in slice culture decreases AMPAR levels at excitatory synapses (19, 21, 22, 29), while mice bearing a GEF1-deficient *Trio* allele exhibited decreased gamma-aminobutyric acid receptor (GABAR)- and glycine receptor (GlyR)-mediated inhibitory miniature current (mIPSC) frequencies in the prefrontal cortex (20). To explore how *Trio* variants impact synaptic function, we measured both miniature excitatory currents (mEPSCs) and mIPSCs in M1 L5 PNs in each of the *Trio* variant heterozygotes.

AMPAR-mediated mEPSC amplitudes were significantly increased in *+/K1431M* and *+/K1918X* mice relative to WT littermates, with no change in their frequencies **(Fig. 4A-C)**. In contrast, AMPAR-mediated mEPSC amplitudes were unchanged in *+/M2145T* mice, but their frequencies were significantly increased. No significant changes in NMDAR mEPSC amplitudes were noted, while NMDAR mEPSCs frequencies were decreased in *+/K1431M* and increased in *+/M2145T* mice cortex **(Fig. 4D-F)**. Notably, these findings correlated with gross alterations in the ratio of NMDAR/AMPAR-mediated evoked (e)EPSCs measured in M1 L5 PNs following stimulation in L2/3. All *Trio* variant heterozygotes showed decreased NMDA/AMPA ratios, indicating imbalances in NMDAR- versus AMPAR-mediated conductance **(Supp. Fig. 4A,B)**. Significant decreases in mIPSC frequencies were noted in

+/K1431M and *+/M2145T* mice relative to WT mice, with no change in amplitudes **(Fig. 4G-I)**. *+/K1918X* mice exhibited increased mIPSC amplitude with no observed change in mIPSC frequency. Together, these data indicate that the *Trio* variants differentially impact excitatory and inhibitory transmission.

Finally, we tested the ability of the L5 PNs to undergo long-term potentiation (LTP) following theta-burst stimulation of L2/3 afferents **(Fig. 4J,K)**. While LTP was robustly induced and potentiated in M1 L5 PNs from WT mice, LTP induction and potentiation were deficient in slices from *+/K1918X* and *+/K1431M* mutant mice. In contrast, *+/M2145T* L5 PNs showed increased induction and prolonged potentiation of LTP compared to WT L5 PNs.

Neurotransmitter release is altered in *Trio +/K1431M* and *+/M2145T* heterozygotes.

In addition to its postsynaptic roles, Trio localizes presynaptically and interacts with the presynaptic active zone scaffolding proteins Bassoon and Piccolo (14, 15, 22). To assess the impact of *Trio* variants on presynaptic function, we first measured the paired-pulse ratio (PPR). Synapses with low probability of release (Pr), *e.g.* L2/3 synapses onto L5 PNs, can undergo paired-pulse facilitation (PPF), a relative increase of synaptic transmission in response to the second of two closely-apposed stimuli. WT and *+/K1918X* M1 L5 PNs exhibited normal facilitation of eEPSC amplitudes that decreased with increased interstimulus interval (ISI) **(Fig. 5A,B)**. PPF was significantly enhanced in *+/K1431M* M1 L5 PNs at short ISIs relative to WT, suggesting a possible reduction in glutamate Pr **(Fig. 5A,B).** The *+/M2145T* PPR curve was unusual, with significantly reduced PPF at short ISIs, yet clearly increased PPF at longer ISI **(Fig. 5A,B)** compared to WT. The decreased PPF at initial ISI in *+/M2145T* mice correlated with increased mEPSC frequency **(Fig. 4A-C)**, suggestive of a possible increase in spontaneous glutamate Pr.

We used high frequency (40Hz) stimulation (HFS) trains to quantitatively estimate glutamate Pr, RRP size, and rates of SV depletion and recovery. A plot of the normalized eEPSC responses to a HFS train stimulation again revealed facilitation upon the first 2-3 stimulations that was increased in *+/K1431M* and decreased in *+/M2145T* slices relative to WT, with no changes in *+/K1918X* slices (**Fig. 5C,D**). Initial facilitation was followed by decaying eEPSC amplitudes, reflecting SV depletion under HFS. All *Trio* variants exhibited a slower train decay rate relative to WT during HFS with *+/M2145T* depleting at half the rate of WT (τ_d, 4.8 s vs WT: 2.7 s) **(Fig. 5D)**.

We used a 'Decay' method (42, 43) to estimate Pr and RRP size from HFS trains. Glutamate Pr in the L2/3-L5 synapses was increased in *+/M2145T* mice, while it was decreased for

+/K1431M mice **(Fig. 5E)**, consistent with the relative changes observed in PPF for these mice. RRP size was much larger in L2/3-L5 synapses of *+/M2145T* mice relative to WT **(Fig. 5F)**, consistent with the increased SV distribution found in close apposition to the AZ **(Fig. 3F,G)**. We tested the ability of the *Trio* variant heterozygotes to recover after train depletion by pairing HFS trains with a single stimulus at increasing intervals (0.01, 2, 6, 9, 12, 18s). The recovery rate (τ_R) was significantly slower in *+/K1431M* L5 PNs and they did not recover to their initial strength within 18 s, plateauing at 78% of maximal recovery compared to WT **(Fig. 5G)**. This modeled increase in glutamate Pr in *+/M2145T* slices was consistent with the measured increase in AMPAR mEPSC frequency.

Trio variant cortex display different proteomic signatures

We used comparative proteomics from P21 cortex to identify proteins and pathways that were differentially altered by the *Trio* variants. We quantified a total of 7,362 proteins, finding distinct difference in the cortical proteome for each genotype **(Supp. Fig. 5, Supp. Table 2)**. Gene Set Enrichment Analysis (GSEA) (45, 46) revealed alterations in distinct functions for each *Trio* variant **(Fig. 6A)**. Of note, the only enriched gene set specific to neurons was downregulation of the synaptic vesicle pathway in *+/K1431M* cortex; all other gene sets were not cell type-specific.

We used SynGo (47) to investigate whether the *Trio* variants impacted synaptic functions. 1,067 of the 7,362 total quantified proteins were synaptic proteins listed in the SynGO geneset. When restricted to brain-specific genes, all three *Trio* variant heterozygotes showed enrichment of differentially expressed proteins (DEPs) in synaptic processes. Notably, *+/M2145T* upregulated DEPs and *+/K1431M* downregulated DEPs were significantly enriched at the presynapse, but with only *+/K1431M* downregulated DEPs showing significant enrichment for postsynaptic neurotransmitter receptor and synaptic vesicle cycling **(Fig. 6B,C)**. Together, our proteomics data point to a significant deficit in presynaptic function in both *+/K1431M* and *+/M2145T* cortex, as well as a significant effect of *+/K1431M* on postsynaptic function.

Rho GEFs and synaptic regulatory proteins are altered in *Trio +/K1431M* and *+/M2145T* heterozygotes.

Given our findings from proteomic analysis and electrophysiology, we measured levels of key presynaptic regulators, including synaptophysin (Syp), syntaxin binding protein1 (Stxbp1, also known as Munc18-1), syntaxin1a (Stx1a) and synaptotagmin3 (Syt3), which are crucial for synaptic vesicle (SV) tethering, docking, replenishment, and calcium-dependent replenishment, respectively. We also measured levels of presynaptic proteins in P42 cortical

synaptosomes, where these proteins are enriched. Munc18-1, Syt3, and Syp levels were increased in *+/M2145T* synaptosomes relative to WT **(Fig. 6D-H)**. Meanwhile, Stx1a levels were significantly decreased in *+/K1431M* synaptosomes compared to WT, with no significant changes in *+/K1918X* compared to WT mice.

The elevated Rac1 activity in *+/K1431M* brain lysates and synaptosomes **(Fig. 1I)** seemed at odds with previous reports that K1431M reduces TRIO GEF1 activity **(Supp. Fig. 1A,B)** (20, 24, 29). We hypothesized that homeostatic compensation in *+/K1431M* mice may alter expression of other RhoGEFs and GAPs. Indeed, levels of the Rac1 GEF Tiam1 were increased in both *+/K1431M* and *+/M2145T* P42 cortical lysates, while VAV2 levels were increased in *+/M2145T* P42 lysates **(Fig. 6I-L)**. Levels of the Trio paralog Kalirin (58) were unaffected in the *Trio* variant mice at P42. Together, our proteomic analyses suggest that presynaptic functions are altered in *+/K1431M* and *+/M2145T* mice and may be driven by abnormal levels of crucial presynaptic regulatory proteins and changes in Rac1 and RhoA activity.

NSC23766, a Rac1-specific inhibitor, rescues neurotransmitter release in *Trio +/K1431M* heterozygotes

Rac1 negatively regulates synaptic vesicle replenishment and synaptic strength in excitatory synapses (15, 44). Rac1 activity was increased while Stx1a levels were decreased in *+/K1431M* cortex, in association with reduced synaptic strength and deficient vesicle replenishment in L2/3-L5 cortical synapses. We tested if acute application of the Rac1 inhibitor NSC23766 (NSC) could rescue these deficits. Treatment of *+/K1431M* slices acutely with NSC normalized PPR in M1 L5 PNs at all ISIs to a WT pattern, suggesting a rescue of the decreased Pr **(Fig. 5A,B).** Application of NSC to *+/K1431M* slices also decreased time to depletion of signal upon high frequency stimulation **(Fig. 5C,D)** and significantly increased Pr without effect on RRP size **(Fig. 5E,F)**, consistent with prior work showing that changes in Rac1 signaling does not impact the RRP (15, 44, 59). Finally, we tested if acute Rac1 inhibition impacts the rate of recovery of the RRP following HFS train stimulation. The recovery curve exhibited improvement at later intervals with full recovery at 18s interval under NSC treatment, but while the recovery rate (τ_R) measured was improved, it remained significantly slower compared to WT **(Fig. 5G).** Overall, we demonstrate that presynaptic Trio GEF1-dependent Rac1 signaling is crucial for maintaining synchronous glutamate Pr and SV replenishment at cortical L2/3-L5 synapses.

DISCUSSION

Large-scale genetic studies show significant overlap in risk genes for ASD, SCZ, and BPD, many converging on synaptic proteins (60-68). However, how variants in a single gene contribute to different NDDs remains a major unresolved question. Our study of mice heterozygous for *Trio* variants associated with ASD (*+/K1431M*), SCZ (*+/K1918X*), and BPD *(+/M2145T*) revealed that the lesions differentially affect Trio protein levels or GEF activity, yielding overlapping but distinct behavioral, neuroanatomical, and synaptic phenotypes. Our findings extend prior work demonstrating that Trio is critical for postsynaptic signaling and synaptic plasticity. We also demonstrate for the first time in mouse model that Trio is critical for glutamate release and synaptic vesicle recycling, and that NDD-associated variants differentially impact these pre- and post-synaptic roles.

Heterozygosity for *Trio* variants in mice yields phenotypes similar to those observed in NDDs

Individuals with mutations in *TRIO* present with a range of neurodevelopmental disorder-associated clinical features, including varying degrees of intellectual disability, altered head size, skeletal and facial features, and behavioral abnormalities (23, 25-28, 33, 69). Patients with missense or truncating variants in *TRIO* that reduce GEF1 activity have mild developmental delay and microcephaly (25, 26, 28, 33). Similarly, we found that heterozygosity for the GEF1-deficient *K1431M* missense or the *K1918X* nonsense variants significantly reduced brain weight and/or head size compared to WT mice, along with multiple behavioral impairments. Notably, while both showed impaired motor coordination and learning, only mice bearing the ASD-associated *K1431M* allele exhibited social interaction deficits.

Both *+/K1431M* and *+/K1918X* adult mice had reduced brain-to-body weight ratios compared to WT, but these were driven by different factors. The smaller brain size in *+/K1918X* mice was associated with a reduction in neuropil and reduced cortical thickness, similar to mice bearing excitatory neuron-specific ablation of one *Trio* allele (19) and paralleling the reduced gray matter volume and cortical thickness in patients with schizophrenia (70-74). Meanwhile, *+/K1431M* mice exhibited an overall increase in body weight leading to relatively decreased head width- and brain-to-body weight ratios in these mice. Adult *+/K1431M* mice had no change in neuropil or cross-sectional brain area, consistent with a prior study describing normal brain size in *+/K1431M* and *K1431M/K1431M* mice at E14.5 (20). Rac1 mediates glucose-stimulated insulin secretion from pancreatic islet beta-cells (75-80), which may explain how chronic alterations in Rac1 activity contribute to weight changes in *Trio +/K1431M* and *+/K1918X* mice. Most studies of *Trio* variants have focused on neuronal effects, but

expression of *Trio* in other tissues could explain the increased body weight in these mice, as well as the musculoskeletal abnormalities associated with *TRIO* variation in humans (23, 25, 27, 32).

Trio variants differentially impact dendritic arbor structure

Rac1 and RhoA signaling is critical for dendrite development (10-13, 81). We found relatively subtle effects of Rac1/RhoA-altering *Trio* variants on cortical L5 PN dendrites. The reductions in dendritic arborization and length in *+/K1918X* neurons are consistent with reports of reduced gray matter volume and dendrite alterations in individuals with schizophrenia versus controls (82, 83), but were modest compared to *NEX-Trio*$^{+/fl}$ mice lacking one copy of Trio in excitatory neurons (19). Reduced Trio function in other cell types, such as in inhibitory neurons or glia, or in neurons from other brain regions that project to cortical M1 L5 PNs, may ameliorate the phenotypes in excitatory neurons of *+/K1918X* relative to *NEX-Trio*$^{+/fl}$ mice. In addition, changes to L5 PN dendrites in *Trio* variant mice appeared to be regionally selective within the arbor: *+/K1431M* neurons had increased arborization only in proximal basal dendrites, while *+/M2145T* neurons had decreased arborization only in the most distal apical dendrites. These differences may reflect the differential spatiotemporal influence of Trio in regulating Rac1 versus RhoA activity. Alternatively, given our finding for presynaptic roles for Trio, these differences may reflect differential effects of the *Trio* variants on both excitatory and inhibitory afferent synaptic inputs which play critical roles in shaping the apical and basal dendrites of L5 PNs (84).

Trio variants impact brain Rho GTPase signaling.

We show here that the *K1431M* variant significantly reduces TRIO GEF1 nucleotide exchange on Rac1 in vitro, consistent with previous reports (24, 29). Decreased Rac1 activity was observed in *+/K1431M* mice at embryonic day 14.5 in the ganglionic eminence, which is enriched for pre-migratory GABAergic interneurons (20). In contrast, we show an increase in active Rac1 levels in *+/K1431M* postnatal brains (at P0, P21, P42) and synaptosomes (at P42) from cortex, primarily composed of differentiated excitatory neurons. This increase aligns with observed phenotypes (e.g. reduced Pr) and reveals why reductions in brain volume, dendrites and spines, or AMPAR signaling anticipated from reduced Rac1 activity (85-89) were not observed in *+/K1431M* mice**.** We propose that the increased Rac1 activity we observed reflects homeostatic compensation in Rac1 regulation occurring between birth to adult ages, and identify changes in Rac1-specific GEFs, e.g. Tiam1 and Vav2, that may contribute to this compensation. Importantly, we did not find changes in Kalirin levels in the adult brain of these Trio mutant mice, suggesting that Kalirin does not compensate for loss of Trio GEF1 activity at this age.

We observed a significant reduction in active RhoA only in purified synaptosomes of *+/M2145T* brains, reflecting the synaptic compartment as a key locus of Trio function. In addition, despite *+/K1918X* mice having half the WT levels of Trio protein, we measured little to no change in active Rac1 and RhoA levels in *+/K1918X* brains. These findings are consistent with recent evidence that the spatiotemporally precise balance of Rac/Rho activity rather than absolute activity levels can mediate cytoskeletal rearrangements (7, 9, 90, 91). Alterations in the activity of additional potential TRIO substrates, such as RhoG (92), Cdc42 (6), and the neurodevelopmentally critical Rac3 (93-95) could also contribute phenotypes in these mice.

The NDD-associated *Trio* variants cause synaptic transmission, plasticity and excitatory/inhibitory imbalance.

Overexpression of a TRIO *K1431M* variant with reduced GEF1 activity decreased AMPAR-mediated mESPC amplitudes in rat organotypic slices (21), while Rac1 activation increased AMPAR amplitudes by promoting synaptic AMPAR clustering (89). In *+/K1431M* mice we observed increased AMPAR current amplitudes without significant changes in NMDAR ESPC amplitudes in evoked and miniature EPSCs recordings, consistent with the increase in active Rac1 levels measured in synaptosomes of adult *+/K1431M* mice. AMPAR EPSC amplitudes were also increased in L5 PNs of *+/K1918X* mice, which have decreased Rac1 activity at P0 and normalized levels of Rac1 by P21 and P42 compared to WT. This temporal increase of Rac1 activity could be enough to drive a subtle but significant increase in AMPAR tone in *+/K1918X*.

mIPSC frequencies were decreased in *+/K1431M* and *+/M2145T* L5 PNs, while mIPSC amplitude was increased in *+/K1918X* slices. Sun et al. noted a similar deficit in inhibitory function in *+/K1431M* prefrontal cortex correlated with reduced interneuron migration to this region, including parvalbumin positive (PV+) neurons (20). In contrast, we did not observe reduced PV+ interneuron numbers in the motor cortex in any *Trio* variant mice, suggesting that *Trio* variants may impact the number of inhibitory synapses or transmission properties rather than solely interneuron migration. Overall, heterozygosity for *Trio* variants dysregulates excitatory and inhibitory synaptic transmission in different patterns, resulting in E/I imbalance, a known driver of NDD phenotypes.

Trio-deficient excitatory neurons are unable to undergo long-term potentiation (LTP) in mouse brain slices (19), which is crucial for working memory in mammals. During LTP ability of Rac1 suggested to be transiently activated and deactivated to regulate AMPAR (96-98). Both

+/K1431M and *+/K1918X* L5 PNs exhibited reduced LTP induction and maintenance. The increased AMPAR resulting from already elevated Rac1 activity (*+/K1431M* mice) or the inability of reduced levels Trio levels to activate Rac1 (*+/K1918X* mice) may preclude LTP in these mice. *+/M2145T* mice showed a striking increase in the induction and maintenance of LTP, correlating with an increased glutamate Pr and SV pool size. The function of RhoA function in plasticity is unknown, but the decrease in RhoA activity measured in cortical synaptosomes may underlie the increase in LTP.

Trio GEF1 and GEF2-deficient variants lead to opposing defects in synaptic release of glutamate.

In neuroendocrine, pancreatic beta, and mast cells, Trio GEF1 activity, Rac1 and RhoA are required for regulation of exocytosis (99-103). Recent work suggest that Trio GEF1 can act through Rac1 to regulate presynaptic processes – Rac1 colocalizes with SVs in the axonal boutons to negatively regulate action potential-dependent (synchronous) glutamate Pr and SV replenishment (15, 44, 59, 104). Using the Rac1 inhibitor NSC, we demonstrate that elevated Rac1 activity, possibly due to Tiam1 upregulation, underlies the reduction in synchronous glutamate Pr and SV replenishment without affecting RRP in *+/K1431M* mice.

Recent work on Rac1 knockout models shows conflicting results regarding their impact on spontaneous (action potential-independent) glutamate Pr, which is critical in synaptogenesis and plasticity (105, 106). Knockout of Rac1 at the Drosophila neuromuscular junction or in cultured mouse hippocampal neurons does not affect the frequency of spontaneous release (15, 59). However, conditional knock out of Rac1 in the Calyx of Held increased spontaneous Pr (44), aligning with the hypothesis that Rac1 activity negatively regulates neurotransmitter release by increasing assembly of actin filaments at the AZ that impede SV fusion. A significant decrease in NMDAR mEPSC frequency in *+/K1431M* mice suggests defects in spontaneous glutamate Pr in cortical synapses, consistent with increased Rac1 activity, while the increase in miniature AMPAR amplitudes could mask the decrease in AMPAR frequency. This relative impact of Rac1 on spontaneous release may reflect functional differences between these diverse synapse types.

RhoA activity is significantly reduced in cortical synaptosomes of *+/M2145T* mice, and this is associated with increased RRP size. While a specific function for RhoA in regulating presynaptic release is currently unclear, levels of Munc18, Syp, and Syt3, are all increased in *+/M2145T* mice and may contribute to the enhanced Pr and altered SV cycling. Taken together, we demonstrate that Trio GEF1 and GEF2 activities play crucial, distinct roles in the presynaptic SV cycle.

Conclusions

TRIO is a risk gene for several NDDs with different patterns of variants observed in different disorders. We show here that variants in *Trio* that lead to impaired Trio levels or GEF function cause both shared and distinct defects in behavior, neuroanatomy, and synaptic function that reflect variant-specific NDD clinical phenotypes. Our data also demonstrate, for the first time, the differential impact of distinct *Trio* lesions on glutamate Pr and SVs replenishment, along with alterations in presynaptic release machinery that contribute to these deficits. We propose that distinct Trio variants act via diverse mechanisms to disrupt normal brain function at the synaptic, circuit, and behavior level.

ACKNOWLEDGEMENTS

We are grateful to Xianyun Ye, Suxia Bai, Andrew Boulton, Chris Kaliszewski, and Xiao-Yuan Li for expert technical support and Bruce Herring, Dick Mains and Betty Eipper for formative discussions.

This work was supported by AHA Postdoctoral Training Grant 20POST35210428 (Y.I.), NIH Medical Scientist Training Program Training Grant T32GM136651 (A.T.J), NIH grants R56MH122449 (A.J.K.), R01MH133562 (A.J.K.), R01MH132685 (A.J.K.) and a Pilot Award from the Simons Foundation.

AUTHOR CONTRIBUTION

YI, ATJ and AJK designed the study and wrote the manuscript. ATJ, TN, and AJK designed alleles and CRISPR strategy and AJK screened pups for germline transmission. TN and the Yale Genome Editing Center generated *Trio* CRISPR alleles. YI designed, conducted and analyzed all electrophysiology experiments. ATJ conducted dendrite reconstructions, dendritic spine analysis, measured brain and body weight, isolated crude synaptosomes and performed GLISAs. SF performed and analyzed all behavioral tests. ATJ collected samples; CMR, KN, and SAM measured protein levels in brain tissue. EEC perfused animals, CAG provided support, and ATJ and YI analyzed images from electron microscopy experiments. YI and ATJ conducted immunoblots and analysis. ATJ conducted Nissl stain and fluorescent immunohistochemistry; ATJ and MJV performed IHC analysis. MGC conducted GEF assays.

CONFLICT OF INTEREST

Authors declare no conflict of interest.

FIGURES

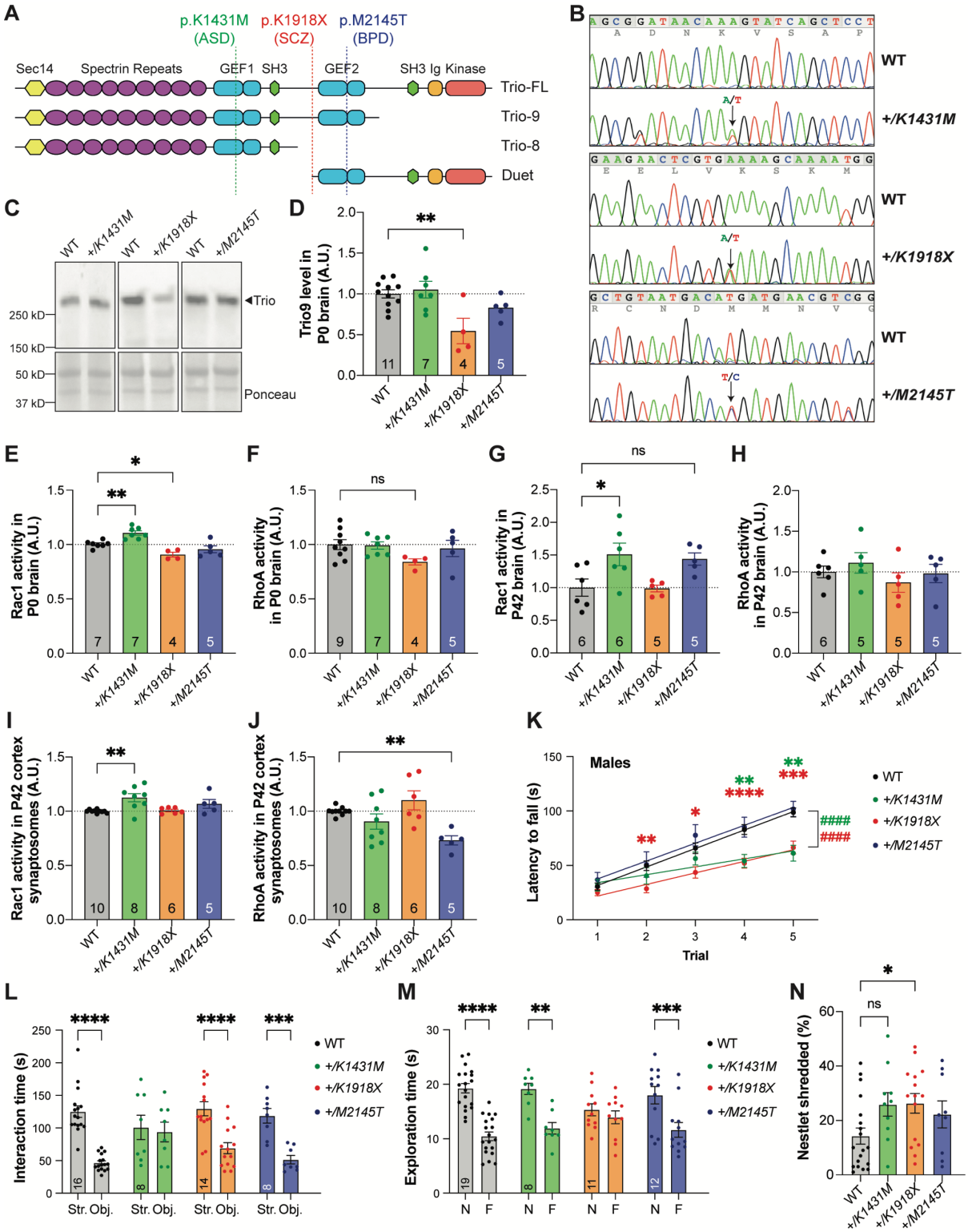

Fig. 1. Genetically engineered mice with heterozygosity for *K1431M*, *K1918X*, or *M2145T* *Trio* variants have divergent effects on Trio protein expression, Rho GTPase activity, and NDD-like behaviors.

(A) Schematic of major Trio isoforms present in the adult mouse brain, with locations of engineered neurodevelopmental disease (NDD)-associated *Trio* variants: *K1431M* autism spectrum disorder (ASD)-associated missense variant in the GEF1 DH domain; *K1918X* schizophrenia (SCZ)-associated nonsense variant that lies just before the GEF2 domain; and *M2145T* bipolar disorder (BPD)-associated missense variant in the GEF2 DH domain. **(B)** Representative sequencing chromatograms of wild-type (WT), *+/K1431M*, *+/K1918X*, and *+/M2145T* mice. Arrows indicate heterozygosity for the variant alleles. **(C)** Representative immunoblots for Trio in P0 brain lysates using an antibody against Trio spectrin repeats (SR5-6). **(D)** Quantification of Trio protein levels from P0 brain lysates. Trio protein levels are reduced only in the brains of *+/K1918X* mice compared to WT controls (0.545 ±0.126 of WT level, p=0.0046). **(E-H)** Activity levels of Rac1 (**E,G**) and RhoA (**F,H**) in whole brain homogenates of neonate (P0, **E-F**) and adult (P42, **G-H**) *Trio* variant mice as measured by G-LISA assay. Rac1 activity is increased in *+/K1431M* mice relative to WT at both ages (1.106 ±0.027-fold at P0, p=0.0035; 1.509 ±0.175-fold at P42, p=0.0279) and decreased in neonate *+/K1918X* mice (0.908 ±0.0.032-fold, p=0.0230), with a trend towards increased activity in adult *+/M2145T* mice (1.438 ±0.183-fold, p=0.0843); meanwhile RhoA activity appears unchanged in all mice relative to WT, though there may be a trend towards decreased activity in *+/K1918X* neonates (0.840 ±0.074-fold, p=0.1292). **(I,J)** Activity levels of Rac1 (**I**) and RhoA (**J**) in synaptosomes isolated from P42 mouse cortex. Rac1 activity is increased in *+/K1431M* synaptosomes (1.125 ±0.107-fold, p=0.0023), while RhoA activity is decreased in *+/M2145T* synaptosomes (0.731 ±0.042-fold, p=0.0093) relative to WT. Data are presented as mean ±SEM. For **(D-J)**, one-way ANOVA with post-hoc Bonferroni MC test identified differences from WT (^{ns}p<0.1, *p<0.05, **p<0.01). Numbers of mice quantified per group are annotated inside the bar. **(K)** *+/K1431M* and *+/K1918X* male mice had decreased latency to fall off an accelerating rotarod compared to WT male mice. Two-way ANOVA with post-hoc Bonferroni MC test identified differences from WT for each individual trial (*p<0.05, **p<0.01, ***p<0.001, ****p<0.0001). Linear regressions identified differences from WT in slopes (WT 16.96 ±1.344; *+/K1431M* 7.270 ±2.019, p<0.0001; *+/K1918X* 10.61 ±1.444, p<0.0001; $^{####}$p<0.0001). n=40 WT; 10 *+/K1431M*; 16 *+/K1918X*; 13 *+/M2145T* male mice. **(L)** WT mice displayed normal social preference and spent more time with a stranger mouse (Str.) relative to an inanimate object (Obj.) in a three-chamber interaction test. Social interactions were impaired in *+/K1431M* male mice. **(M)** WT mice spent more time with a novel object (N) than with a familiar object (F). Novel object recognition was impaired in *+/K1918X* male mice. All data are presented as mean ±SEM. For **(L-M)**, two-way ANOVA with post-hoc Bonferroni MC test

identified differences from WT (^{ns}p<0.1, *p<0.05, **p<0.01, ***p<0.001, ****p<0.0001). Numbers of mice quantified per group are annotated inside the bar. **(N)** Male *+/K1918X* mice exhibited increased nestlet shredding over 30 min (26.26 ±3.61% shredded vs WT 14.26 ±2.97%; p=0.0433), and *+/K1431M* mice exhibited a trend toward increased nestlet shredding (25.90 ±4.34% shredded, p=0.1038) compared to WT mice. One-way ANOVA with post-hoc Bonferroni MC test identified differences from WT (^{ns}p<0.1, *p<0.05). n=19 WT; 10 *+/K1431M*; 15]*+/K1918X*; 9 *+/M2145T* male mice.

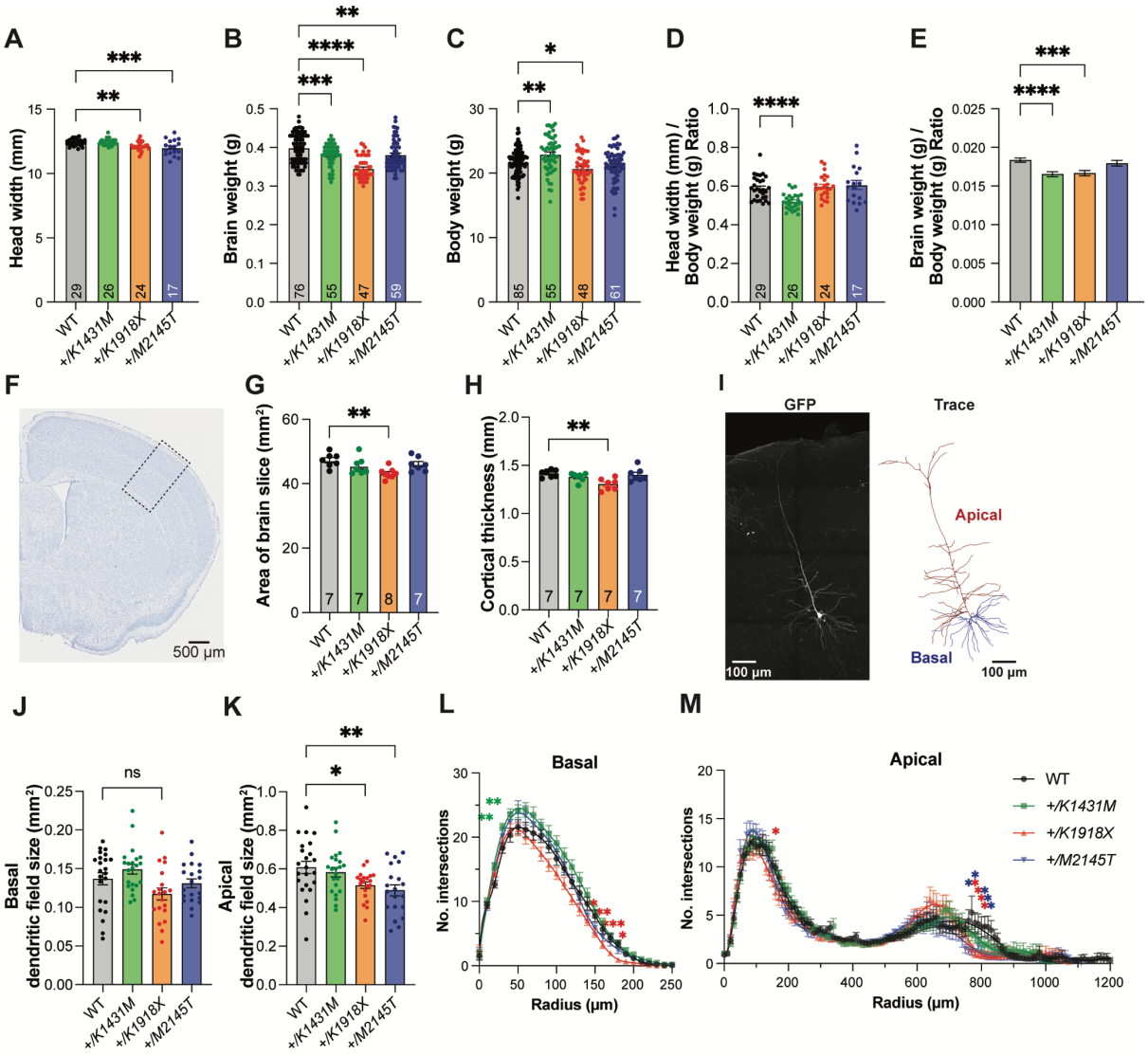

Fig. 2. *Trio +/K1431M* and *+/K1918X* mice have smaller brain weights, but only *+/K1918X* brains have smaller less complex neurons.

(A) Ear-to-ear head width is reduced in P42 *+/K1918X* and *+/M2145T* compared to WT male mice (*+/K1918X* 12.125 ±0.074 mm, p=0.0096; *+/M2145T* 12.012 ±0.152 mm, p=0.0007; vs WT 12.414 ±0.049 mm). **(B)** Brain weight is significantly reduced in P42 *+/K1431M*, *+/K1918X*, and *+/M2145T* males compared to WT (*+/K1431M* 0.379 ±0.004 g, p=0.0006; *+/K1918X* 0.345

±0.004 g, p<0.0001; *+/M2145T* 0.381 ±0.005 g, p=0.0016; vs WT 0.399 ±0.004 g). **(C)** Body weight is increased in P42 *+/K1431M* and decreased in *+/K1918X* males (*+/K1431M* 22.911 ±0.382 g, p=0.0034; *+/K1918X* 20.700 ±0.338 g, p=0.0153; vs WT 21.745 ±0.224 g). **(D)** Head widths normalized to body weight of P42 *+/K1431M* male mice were reduced 11.8% compared to WT mice (0.520 ±0.008 mm/g vs WT 0.589 ±0.011 mm/g, p=0.0001). Head width-to-body weight ratios were calculated per individual mouse, with mouse number per group annotated within the bar. **(E)** Brain weights normalized to body weight of P42 *+/K1431M* and *+/K1918X* male mice were reduced 9.9% and 9.2%, resp., compared to WT mice (*+/K1431M* 0.0165 ±0.0004, p=0.0002; *+/K1918X* 0.0167 ±0.0004, p=0.0015; vs WT 0.0184 ±0.0004). Ratios were calculated by dividing the mean brain weight (B) by the mean body weight (C) of overlapping but non-identical populations of mice (see (B) and (C) for mouse number per group). For (**A-E**), data are presented as mean ±SEM; only male mice are shown here (data for females in **Supp. Fig. 2**). One-way ANOVA with post-hoc Bonferroni MC test identified differences from WT (^{ns}p<0.1, *p<0.05, **p<0.01, ***p<0.001, ****p<0.0001; n=number of mice per group, annotated within the bar). **(F)** Representative Nissl-stained image of a 30 µm coronal slice from a P42 WT brain. Magnification of the cortex (dotted black box) reveals cortical layers. **(G)** Total cross-sectional brain area of Nissl-stained coronal sections were reduced ~9% in P42 *+/K1918X* brains (43.21 ±0.577 mm^2 vs WT 47.29 ±0.823 mm^2, p=0.0045). **(H)** Total thickness of the cortex, in the region marked by the dotted black box in (F), is reduced ~8% in P42 *+/K1918X* brains (1.304 ±0.02262 mm vs WT 1.416 ±0.01417 mm, p=0.0021). For (**G,H**), data are presented as mean ±SEM. Ordinary one-way ANOVA with post-hoc Bonferroni MC test identified differences from WT (**p<0.01; n=number of mouse brains, annotated within the bar). **(I)** Representative maximum projection fluorescence image and corresponding dendritic arbor reconstruction of a motor cortex Layer 5 pyramidal neuron (M1 L5 PN) from a WT mouse. **(J,K)** Dendritic field size as measured by convex hull analysis of basal (J) and apical (K) dendrite arbor reconstructions of M1 L5 PNs of P42 *Trio* variant mice. *+/K1918X* trended toward smaller basal dendritic field size (0.1172 ±0.0078 mm^2 vs WT 0.1368 ±0.0077 mm^2, p=0.0933), and both *+/K1918X* and *+/M2145T* had significantly smaller apical dendritic field size (*+/K1918X* 0.5157 ±0.0169 mm^2, p=0.0460; *+/M2145T* 0.4893 ±0.0285 mm^2, p=0.0062; vs WT 0.6081 ±0.0319 mm^2) compared to WT L5 PNsOrdinary one-way ANOVA with post-hoc Bonferroni MC test (B) identified differences from WT (^{ns}p<0.1, *p<0.05, **p<0.01). **(L-M)** Sholl analysis revealed basal (L) and apical (M) dendritic arborization changes in *Trio* variant M1 L5 PNs compared to WT: both basal and apical arborization was reduced in *+/K1918X*, while proximal basal arborization was increased in *+/K1431M*. Two-way ANOVA (stacked) with post-hoc Bonferroni MC test identified differences from WT at each radius centered at the soma (*p<0.05, **p<0.01, ***p<0.001) For (J-M), n=23

neurons from 17 WT mice, 22 neurons from 15 *+/K1431M* mice, 20 neurons from 12 *+/K1918X* mice, 20 neurons from 14 *+/M2145T* mice.

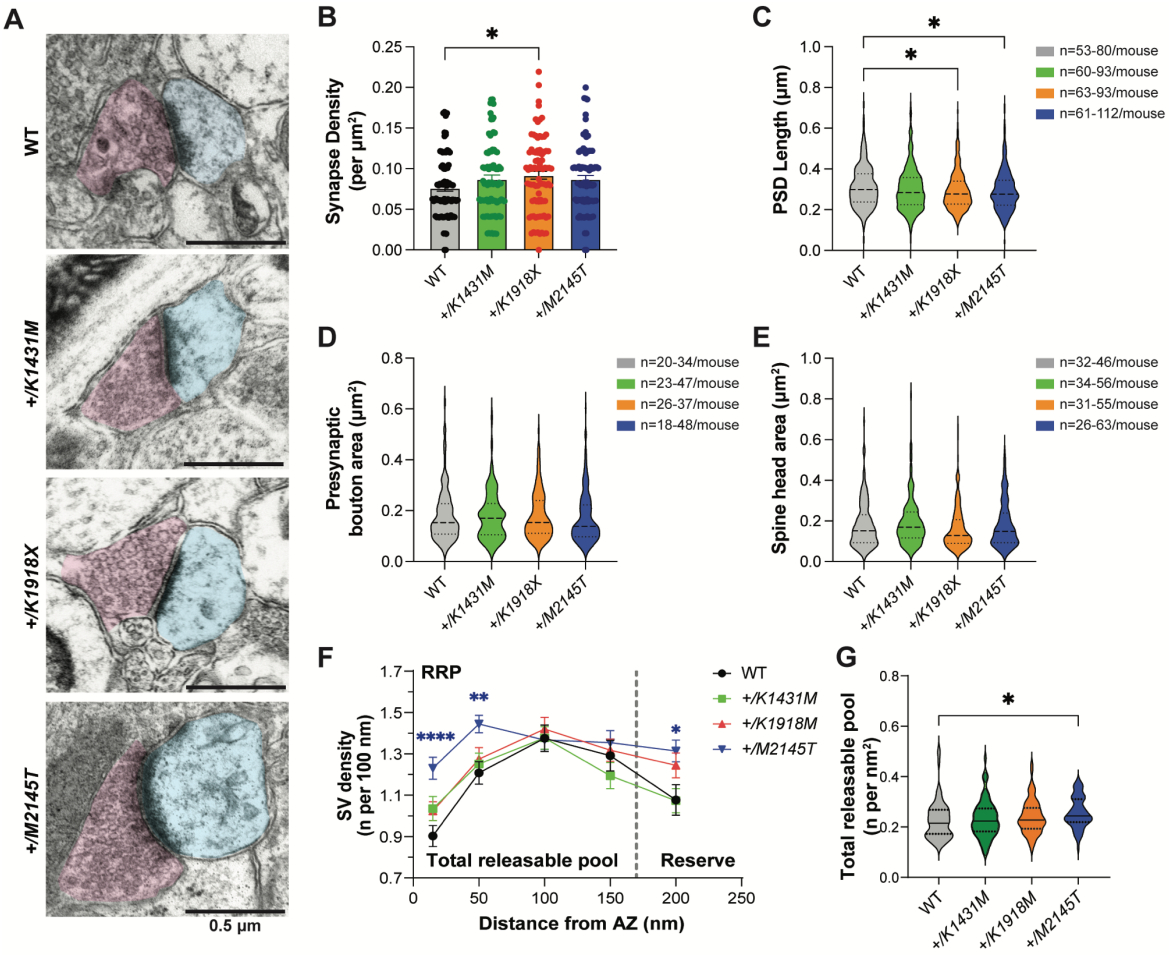

Fig. 3. *Trio* variants differentially impact synapse ultrastructure and synaptic vesicle distribution.

(A) Representative electron micrograph (EM) images from motor cortex layer 5 (M1 L5) of P42 WT and *Trio* variant mice. Post-synaptic regions are pseudo-colored in cyan; pre-synaptic regions in magenta. Scale bar = 0.5 µm. **(B)** Asymmetric synapses from all EM images of M1 L5 were quantified (from 18 fields of view per mouse, 5 mice per group). Synapse density was

increased in *+/K1918X* mice (0.09205 ±0.004775 synapses/um^2; vs WT 0.07633 ±0.003954 synapses/um^2, p=0.0345). **(C)** PSD lengths were decreased in M1 L5 synapses of *+/K1918X* and *+/M2145T* mice (*+/K1918X* 0.2926 ±0.004652 um, p=0.0204; *+/M2145T* 0.2916 ±0.004922 um, p=0.0142; vs WT 0.3125 ±0.005612 um). **(D,E)** Presynaptic bouton and spine head areas of M1 L5 synapses were unchanged from WT in all *Trio* variants. For (C-E), number of measurements per mouse across all 5 mice per genotype are denoted in the corresponding figure. **(F)** Synaptic vesicles (SVs) counted per 100 nm of active zone (AZ) length in M1 L5 as a function of distance from the AZ. *+/M2145T* showed an increase in readily releasable pool (RRP) identified as docked SVs (15 nm from AZ; 1.23 ±0.05 vs WT 0.90 ±0.05) and increase in tethered SVs (50 nm from AZ; 1.44 ±0.04 vs WT 1.20 ± 0.05). *+/K1918X and +/M2145T* also showed an increase in the reserve pool of SVs (200 nm from AZ; 3.51 ±0.21 and 3.81 ±0.18, resp. vs WT 2.74 ±0.16). **(G)** Total releasable pool, calculated as number of SVs at 15-150 nm from AZ per area of distribution (nm^2). RRP was significantly increased in *+/M2145T* (0.257 ±0.007 vs WT 0.228 ±0.008), driven by increased docked and tethered SVs. All data are presented as mean ±SEM. Ordinary one-way ANOVA with post-hoc Bonferroni MC test identified differences from WT (*p<0.05, **p<0.01, ***p<0.001, ****p<0.0001). For (F,G), 35-50 synapses per mouse were analyzed.

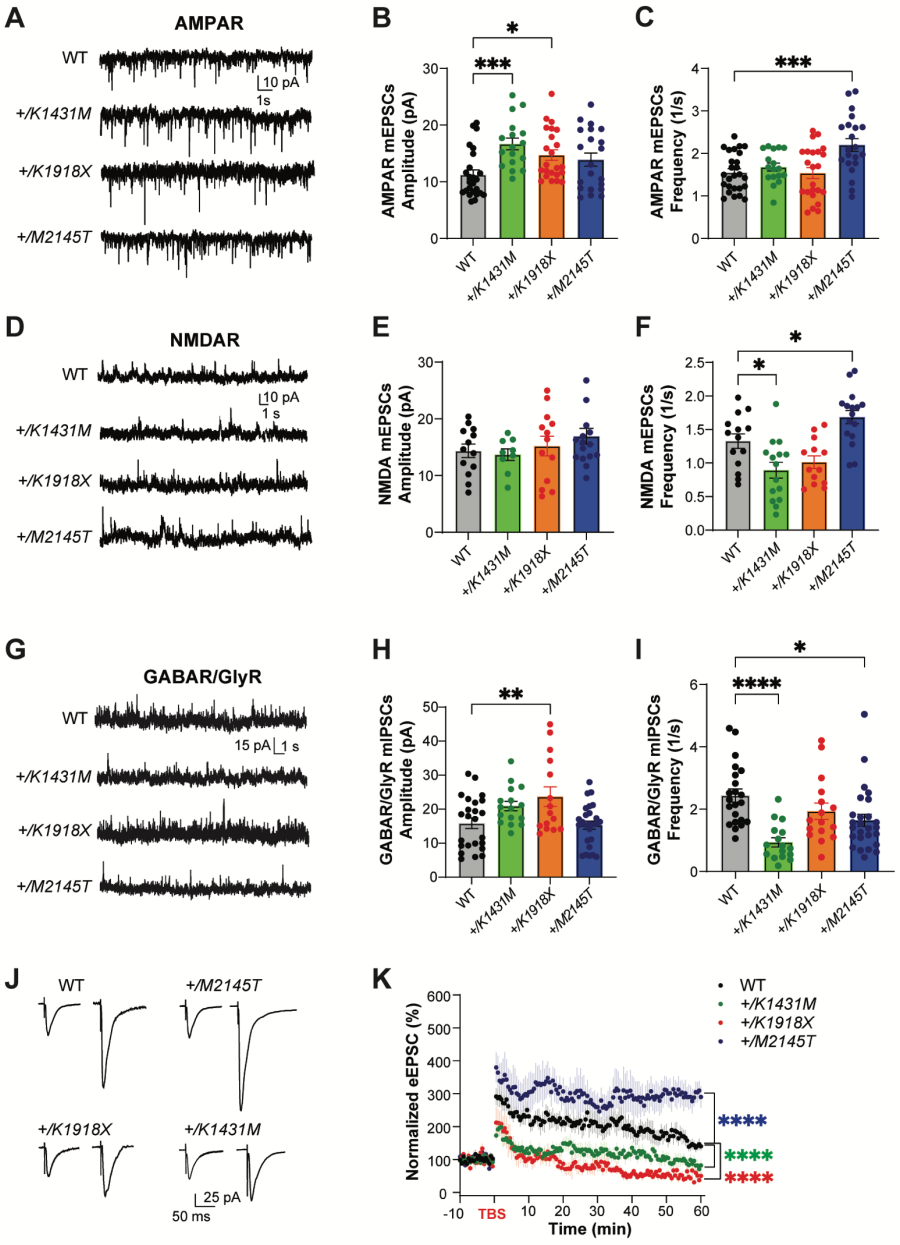

Fig. 4. *Trio* variant mice exhibit deficits in synaptic signaling and LTP.

(A, D) Representative traces of miniature excitatory AMPAR-, NMDAR-mediated mEPSCs and **(G)** inhibitory postsynaptic currents mIPSCs in M1 L5 pyramidal neurons of WT, *+/K1431M*, *+/K1918X* and *+/M2145T* mice. **(B)** AMPAR-mediated mEPSC amplitudes (I) were significantly increased in *+/K1431M* (16.67 ±1.04 pA) and *+/K1918X* (14.71 ±0.92 pA) slices, with no observed changes in *+/M2145T* slices (13.90 ±1.16 pA) compared to WT (11.25 ±0.84

pA; n=17-25 neurons from ≥6-8 mice per group). **(C)** No significant changes in AMPAR mEPSCs frequencies (q) were observed in *+/K1431M* and *+/K1918X,* while *+/M2145T* had an increase (2.20 ±0.15 1/s; vs WT 1.55 ±0.09 1/s). **(E, F)** NMDAR mEPSCs frequencies were reduced in *+/K1431M* (0.89 ±0.12 1/s; vs WT 1.3324 ±0.11 1/s; n=9-13 neurons from ≥5-7 mice per group) and showed a slight but significant increase in *+/M2145T* mice (1.68 ±0.10 1/s). **(H, I)** GABA/GlyR mIPSCs amplitudes were significantly increased in *+/K1918X* vs WT (23.69 ±2.89 pA; vs 15.86 ±1.56 pA, resp.), while frequency was decreased in *+/K1431M* and *+/M2145T* (0.94 ±0.14 1/s and 1.64 ±0.19 1/s resp.; vs WT 2.44 ±0.20; n=16-26 neurons from ≥6-8 mice per group). For **(B-I)**, data are presented as mean ±SEM. One-way ANOVA with post-hoc Bonferroni test identified differences from WT (*p<0.05; **p<0.01; ***p<0.001; ****p<0.0001). **(J)** Averaged representative traces of baseline and post-TBS eEPSCs currents in M1 L5 PNs of WT and *Trio* variant mice. **(K)** Normalized eEPSCs amplitudes measuring LTP in L5 PNs by TBS in L2/3 afferents in all genotypes showed a significant decrease in the initiation and no potentiation of the LTP in *+/K1431M* and *+/K1918X*, with increase in initiation and potentiation of *+/M2145T* M1 L5 PNs compared to WT. LTP was induced at 0 min. RM two-way ANOVA with post-hoc Bonferroni MC test identified differences from WT (****p<0.0001; n=6-8 neurons from ≥4-5 mice per group).

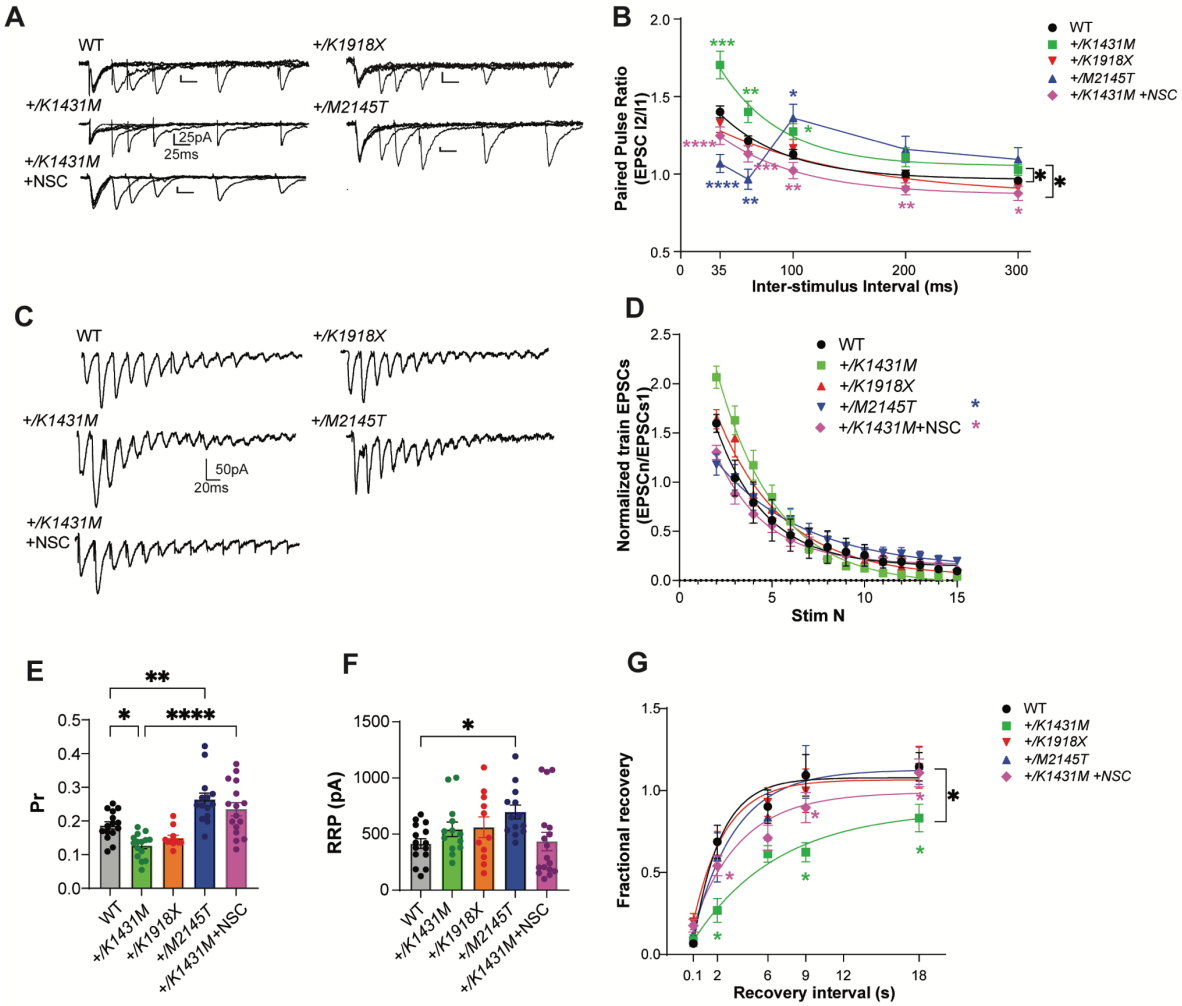

Fig. 5. *Trio* variant mice have deficiencies in short-term facilitation, glutamate Pr and RRP.

(A) Representative traces in M1 L5 PNs of WT, *Trio* variant mice and rescue experiment in acute slices of *+/K1431M* with 100 µM NSC23766 in response to paired pulse stimulation in L2/3. **(B)** Paired-pulse ratio (PPR) at varying interstimulus intervals (ISI), overlaid with a single exponential fit (except for *+/M2145T* data). An increase in the initial PPR was observed in M1

L5 PNs of *+/K1431M* mice (35 ms: 1.70 ±0.089, p=0.003; 60 ms: 1.40 ±0.07, p=0.046; 100 ms: 1.27±0.05, p=0.031; n=20-34 neurons from ≥7-9 mice per group) with no change in *+/K1918X*; and in *+/M2145T* we observed a decrease in initial RRP at shorter ISI (35 ms: 1.05 ±0.06, p<0.0001; 60 ms: 0.97 ±0.06, p=0.037) and an increase in longer ISI (100 ms: 1.36 ±0.09, p=0.034; 200 ms: 1.18 ±0.08, p=0.013) compared to WT (35 ms: 1.40 ±0.04; 60ms: 1.21 ±0.03; 100 ms: 1.13 ±0.03; 200 ms 1.0 ±0.02; 300 ms 0.96 ±0.17). Acute application of NSC onto *+/K1431*M slices significantly shifted the PPR curve at all ISI downwards compared to untreated *+/K1431M*, and showed no significant difference from WT (*+/K1431M* +NSC 35 ms: 1.25 ±0.06, p<0.0001; 60 ms: 1.13 ±0.052, p=0.0007; 100 ms: 1.02 ±0.053, p=0.0017; 200 ms 0.91 ±0.039, p=0.0043; 300 ms 0.88 ±0.045, p=0.021). **(C)** Representative traces of AMPAR eEPSCs in M1 L5 PNs under HFS (15 pulses at 40 Hz) in L2/3. **(D)** AMPAR $eEPSC_n$ amplitudes normalized to $eEPSC_1$ of the train revealed changes in the depletion rates during HFS in *Trio* variants compared to WT (tau decay (τ_d), WT: 2.70 s, *+/K1431M:* 3.19 s, *+/M2145T:* 4.79 s, *+/K1918X:* 3.52 s, *+/K1431M*+NSC*:* 2.68 s; n=12-15 neurons from 5-7 mice). **(E)** The estimated glutamate probability of release (Pr) was decreased in *+/K1431M* (0.13 ±0.099) and increased in *+/M2145T* (0.26 ±0.019), with no significant change in *+/K1918X* (0.15 ±0.01) compared to WT M1 L5 PNs (0.19 ±0.01; n=11-15 neurons from ≥ 5 mice per group); acute NSC application rescued Pr in *+/K1431M* (0.22 ±0.019; n=11-15 neurons from ≥ 5 mice per group). **(F)** The calculated size of the readily releasable vesicle pool (RRP) was increased in *+/M2145T* M1 L5 PNs compared to WT (665.7 ±68.5 pA vs 415.8 ±43.9 pA). RRP in *+/K1431M* synapses before or after treatment with NSC did not differ from WT (543.1±64.4 pA; +NSC: 427.9±79.2 pA vs 415.8 ±43.9 pA) **(G)** Exponential fits of the fractional recovery plotted vs ISI. Time of recovery, measured by exponential tau recovery (τ_R), was significantly decreased in *+/K1431M* M1 L5 PNs (6.3 s, vs WT 1.7 s). *+/K1431M* exhibited an inability to fully recover to initial levels after ISI 18 s, while NSC application have allowed for full recovery at 18s it improved but did not fully rescued tau recovery time in *+/K1431M* (5.2 s). Data are presented as mean ±SEM, with significant differences from WT tested using one-way ANOVA with post-hoc Bonferroni (*p<0.05; **p<0.01; ***p<0.001; ****p<0.0001).

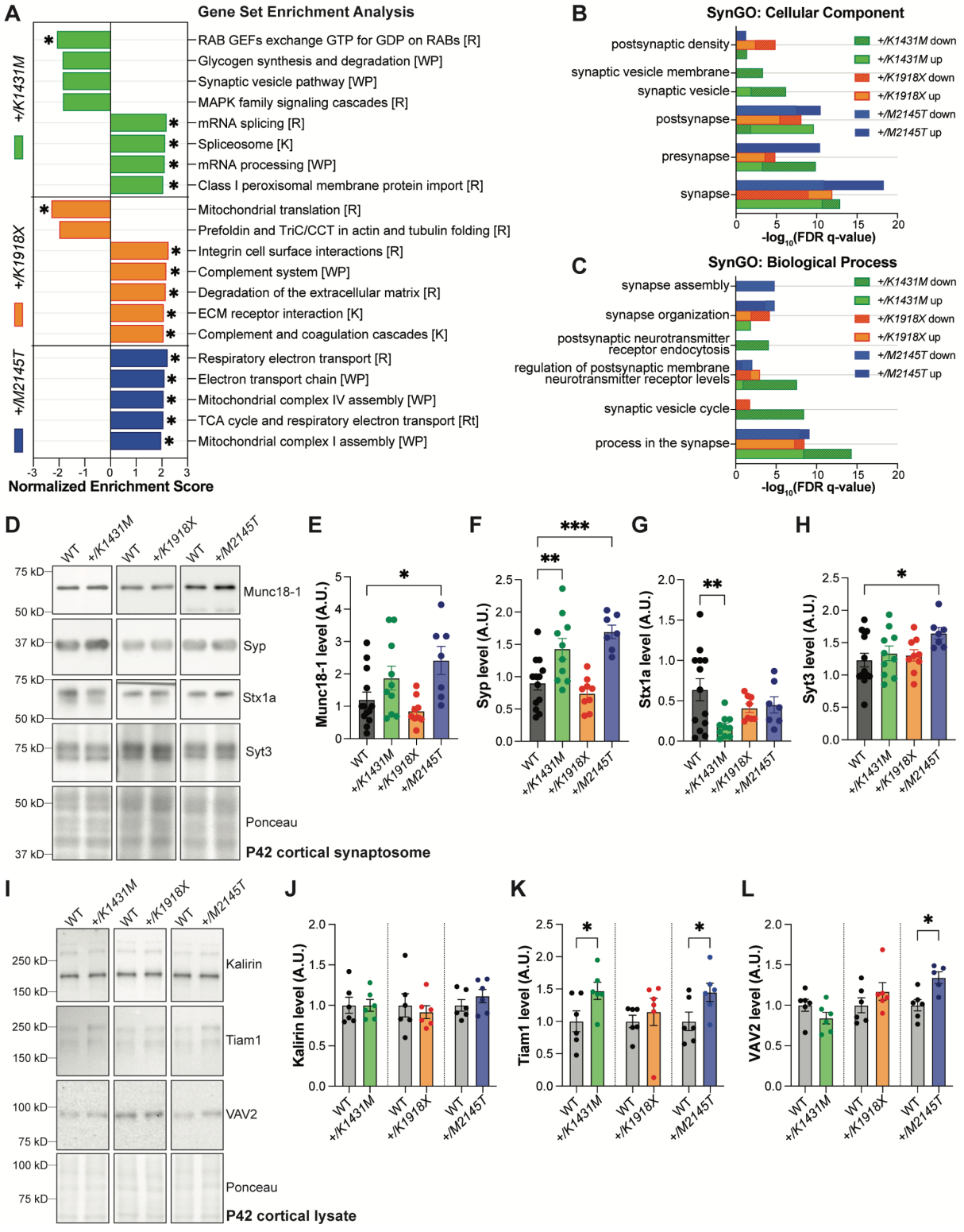

Fig. 6 *Trio* variant mice show different molecular changes in the cortex involving presynaptic machinery and Rac1 GEFs.

(A) Bar graph illustrating the top enriched pathways (FDR q-value<0.2, *FDR<0.05) identified by gene set enrichment analysis (GSEA) for each *Trio* mutant mouse compared to WT, using all proteins quantified by mass spectrometry in P21 cortex (7362 proteins, n=4 mice per genotype), sorted by normalized enrichment score (NES). Pathways with a positive NES are

upregulated compared to WT; pathways with a negative NES are downregulated compared to WT. [ ] denotes the gene set: [R] = Reactome, [WP] = WikiPathways, [K] = KEGG. **(B,C)** Bar graphs illustrating the top enriched (FDR q-value <0.001) **(B)** cellular components and **(C)** biological processes identified by GSEA, using synaptic proteins from SynGO gene sets (n=1077 proteins). For a complete list of all enriched pathways identified by GSEA and SynGO, see Supp. Table 3. **(D)** Representative immunoblots for Munc18-1, synaptophysin (Syp), syntaxin-1a (Stx1a), and synaptotagmin3 (Syt3) in synaptosomes isolated from P42 cortex of WT and *Trio* variant mice. **(E-H)** Normalized intensity levels from immunoblots of select presynaptic proteins from P42 cortical synaptosomes. Munc18-1, Syp, and Syt3 are significantly increased in *+/M2145T* synaptosomes compared to WT; Syp is increased while Stx1a is significantly decreased in *+/K1431M* synaptosomes compared to WT. Ordinary one-way ANOVA with post-hoc Bonferonni MC test identified differences from WT (*p<0.05, **p<0.01, ***p<0.001; n=synaptosomes from 14 WT, 10 *+/K1431M*, 9 *+/K1918X*, and 7 *+/M2145T* male mice). **(I)** Representative immunoblots for Kalirin, Tiam1, and VAV2 in P42 cortical RIPA lysates of WT and *Trio* variant mice. **(J-L)** Normalized intensity levels from immunoblots of select RhoGEFs from P42 cortical lysates. Kalirin levels are unchanged in all *Trio* variant cortex compared to WT; Tiam1 levels are increased ~47% in *+/K1431M* and increased ~45% in *+/M2145T* cortex compared to WT; VAV2 is increased ~34% in *+/M2145T* cortex compared to WT. Unpaired t-tests identified differences from WT (*p<0.05; n=6 mice per genotype).

REFERENCES

1. American Psychiatric Association. Diagnostic and Statistical Manual of Mental Disorders. 5th ed. Washington, DC2013.
2. Anttila V, Bulik-Sullivan B, Finucane HK, Walters RK, Bras J, Duncan L, et al. Analysis of shared heritability in common disorders of the brain. Science. 2018;360(6395):1313-+.
3. Romero C, Werme J, Jansen PR, Gelernter J, Stein MB, Levey D, et al. Exploring the genetic overlap between twelve psychiatric disorders. Nature Genetics. 2022;54(12).
4. Debant A, Serra-Pages C, Seipel K, O'Brien S, Tang M, Park SH, et al. The multidomain protein Trio binds the LAR transmembrane tyrosine phosphatase, contains a protein kinase domain, and has separate rac-specific and rho-specific guanine nucleotide exchange factor domains. Proc Natl Acad Sci U S A. 1996;93(11):5466-71.
5. Bellanger JM, Lazaro JB, Diriong S, Fernandez A, Lamb N, Debant A. The two guanine nucleotide exchange factor domains of Trio link the Rac1 and the RhoA pathways in vivo. Oncogene. 1998;16(2):147-52.
6. Blangy A, Vignal E, Schmidt S, Debant A, Gauthier-Rouviere C, Fort P. TrioGEF1 controls Rac- and Cdc42-dependent cell structures through the direct activation of rhoG. J Cell Sci. 2000;113 (Pt 4):729-39.
7. Grubisha MJ, DeGiosio RA, Wills ZP, Sweet RA. Trio and Kalirin as unique enactors of Rho/Rac spatiotemporal precision. Cell Signal. 2022;98:110416.
8. Paskus JD, Herring BE, Roche KW. Kalirin and Trio: RhoGEFs in Synaptic Transmission, Plasticity, and Complex Brain Disorders. Trends Neurosci. 2020;43(7):505-18.
9. Duman JG, Mulherkar S, Tu YK, J XC, Tolias KF. Mechanisms for spatiotemporal regulation of Rho-GTPase signaling at synapses. Neurosci Lett. 2015;601:4-10.
10. Hall A. Rho GTPases and the actin cytoskeleton. Science. 1998;279(5350):509-14.
11. Luo L. Rho GTPases in neuronal morphogenesis. Nat Rev Neurosci. 2000;1(3):173-80.
12. Nakayama AY, Harms MB, Luo L. Small GTPases Rac and Rho in the maintenance of dendritic spines and branches in hippocampal pyramidal neurons. J Neurosci. 2000;20(14):5329-38.
13. Newey SE, Velamoor V, Govek EE, Van Aelst L. Rho GTPases, dendritic structure, and mental retardation. J Neurobiol. 2005;64(1):58-74.
14. Terry-Lorenzo RT, Torres VI, Wagh D, Galaz J, Swanson SK, Florens L, et al. Trio, a Rho Family GEF, Interacts with the Presynaptic Active Zone Proteins Piccolo and Bassoon. PLoS One. 2016;11(12):e0167535.
15. O'Neil SD, Racz B, Brown WE, Gao Y, Soderblom EJ, Yasuda R, et al. Action potential-coupled Rho GTPase signaling drives presynaptic plasticity. Elife. 2021;10.
16. O'Brien SP, Seipel K, Medley QG, Bronson R, Segal R, Streuli M. Skeletal muscle deformity and neuronal disorder in Trio exchange factor-deficient mouse embryos. Proc Natl Acad Sci U S A. 2000;97(22):12074-8.
17. Peng YJ, He WQ, Tang J, Tao T, Chen C, Gao YQ, et al. Trio is a key guanine nucleotide exchange factor coordinating regulation of the migration and morphogenesis of granule cells in the developing cerebellum. The Journal of biological chemistry. 2010;285(32):24834-44.
18. Zong W, Liu S, Wang X, Zhang J, Zhang T, Liu Z, et al. Trio gene is required for mouse learning ability. Brain Res. 2015;1608:82-90.
19. Katrancha SM, Shaw JE, Zhao AY, Myers SA, Cocco AR, Jeng AT, et al. Trio Haploinsufficiency Causes Neurodevelopmental Disease-Associated Deficits. Cell Rep. 2019;26(10):2805-17 e9.
20. Sun X, Wang L, Wei C, Sun M, Li Q, Meng H, et al. Dysfunction of Trio GEF1 involves in excitatory/inhibitory imbalance and autism-like behaviors through regulation of interneuron migration. Mol Psychiatry. 2021.

21. Tian C, Paskus JD, Fingleton E, Roche KW, Herring BE. Autism Spectrum Disorder/Intellectual Disability-associated mutations in Trio disrupt Neuroligin 1-mediated synaptogenesis. J Neurosci. 2021.
22. Paskus JD, Tian C, Fingleton E, Shen C, Chen X, Li Y, et al. Synaptic Kalirin-7 and Trio Interactomes Reveal a GEF Protein-Dependent Neuroligin-1 Mechanism of Action. Cell Rep. 2019;29(10):2944-52 e5.
23. Ba W, Yan Y, Reijnders MR, Schuurs-Hoeijmakers JH, Feenstra I, Bongers EM, et al. TRIO loss of function is associated with mild intellectual disability and affects dendritic branching and synapse function. Hum Mol Genet. 2016;25(5):892-902.
24. Katrancha SM, Wu Y, Zhu M, Eipper BA, Koleske AJ, Mains RE. Neurodevelopmental disease-associated de novo mutations and rare sequence variants affect TRIO GDP/GTP exchange factor activity. Hum Mol Genet. 2017.
25. Barbosa S, Greville-Heygate S, Bonnet M, Godwin A, Fagotto-Kaufmann C, Kajava AV, et al. Opposite Modulation of RAC1 by Mutations in TRIO Is Associated with Distinct, Domain-Specific Neurodevelopmental Disorders. Am J Hum Genet. 2020;106(3):338-55.
26. Bonnet M, Roche F, Fagotto-Kaufmann C, Gazdagh G, Truong I, Comunale F, et al. Pathogenic TRIO variants associated with neurodevelopmental disorders perturb the molecular regulation of TRIO and axon pathfinding in vivo. Mol Psychiatry. 2023;28(4):1527-44.
27. Gazdagh G, Hunt D, Gonzalez AMC, Rodriguez MP, Chaudhry A, Madruga M, et al. Extending the phenotypes associated with TRIO gene variants in a cohort of 25 patients and review of the literature. Am J Med Genet A. 2023;191(7):1722-40.
28. Pengelly RJ, Greville-Heygate S, Schmidt S, Seaby EG, Jabalameli MR, Mehta SG, et al. Mutations specific to the Rac-GEF domain of TRIO cause intellectual disability and microcephaly. J Med Genet. 2016;53(11):735-42.
29. Sadybekov A, Tian C, Arnesano C, Katritch V, Herring BE. An autism spectrum disorder-related de novo mutation hotspot discovered in the GEF1 domain of Trio. Nat Commun. 2017;8(1):601.
30. Singh T, Poterba T, Curtis D, Akil H, Al Eissa M, Barchas JD, et al. Rare coding variants in ten genes confer substantial risk for schizophrenia. Nature. 2022;604(7906):509-16.
31. Howrigan DP, Rose SA, Samocha KE, Fromer M, Cerrato F, Chen WJ, et al. Exome sequencing in schizophrenia-affected parent-offspring trios reveals risk conferred by protein-coding de novo mutations. Nat Neurosci. 2020;23(2):185-93.
32. Kloth K, Graul-Neumann L, Hermann K, Johannsen J, Bierhals T, Kortum F. More evidence on TRIO missense mutations in the spectrin repeat domain causing severe developmental delay and recognizable facial dysmorphism with macrocephaly. Neurogenetics. 2021;22(3):221-4.
33. Bircher JE, Corcoran EE, Lam TT, Trnka MJ, Koleske AJ. Autoinhibition of the GEF activity of cytoskeletal regulatory protein Trio is disrupted in neurodevelopmental disorder-related genetic variants. The Journal of biological chemistry. 2022;298(9):102361.
34. Frankfurt M, Luine V. The evolving role of dendritic spines and memory: Interaction(s) with estradiol. Horm Behav. 2015;74:28-36.
35. Blaise AM, Corcoran EE, Wattenberg ES, Zhang YL, Cottrell JR, Koleske AJ. In vitro fluorescence assay to measure GDP/GTP exchange of guanine nucleotide exchange factors of Rho family GTPases. Biol Methods Protoc. 2022;7(1):bpab024.
36. Hollingsworth EB, McNeal ET, Burton JL, Williams RJ, Daly JW, Creveling CR. Biochemical characterization of a filtered synaptoneurosome preparation from guinea pig cerebral cortex: cyclic adenosine 3':5'-monophosphate-generating systems, receptors, and enzymes. J Neurosci. 1985;5(8):2240-53.
37. Scheetz AJ, Nairn AC, Constantine-Paton M. NMDA receptor-mediated control of protein synthesis at developing synapses. Nat Neurosci. 2000;3(3):211-6.
38. Levy AD, Xiao X, Shaw JE, Sudarsana Devi SP, Katrancha SM, Bennett AM, et al. Noonan Syndrome-Associated SHP2 Dephosphorylates GluN2B to Regulate NMDA Receptor Function. Cell Rep. 2018;24(6):1523-35.

39. Gonzalez-Forero D, Montero F, Garcia-Morales V, Dominguez G, Gomez-Perez L, Garcia-Verdugo JM, et al. Endogenous Rho-kinase signaling maintains synaptic strength by stabilizing the size of the readily releasable pool of synaptic vesicles. J Neurosci. 2012;32(1):68-84.
40. Montesinos MS, Dong W, Goff K, Das B, Guerrero-Given D, Schmalzigaug R, et al. Presynaptic Deletion of GIT Proteins Results in Increased Synaptic Strength at a Mammalian Central Synapse. Neuron. 2015;88(5):918-25.
41. Dong W, Radulovic T, Goral RO, Thomas C, Suarez Montesinos M, Guerrero-Given D, et al. CAST/ELKS Proteins Control Voltage-Gated Ca(2+) Channel Density and Synaptic Release Probability at a Mammalian Central Synapse. Cell Rep. 2018;24(2):284-93 e6.
42. Ruiz R, Cano R, Casanas JJ, Gaffield MA, Betz WJ, Tabares L. Active zones and the readily releasable pool of synaptic vesicles at the neuromuscular junction of the mouse. J Neurosci. 2011;31(6):2000-8.
43. Thanawala MS, Regehr WG. Determining synaptic parameters using high-frequency activation. J Neurosci Methods. 2016;264:136-52.
44. Keine C, Al-Yaari M, Radulovic T, Thomas CI, Valino Ramos P, Guerrero-Given D, et al. Presynaptic Rac1 controls synaptic strength through the regulation of synaptic vesicle priming. Elife. 2022;11.
45. Subramanian A, Tamayo P, Mootha VK, Mukherjee S, Ebert BL, Gillette MA, et al. Gene set enrichment analysis: a knowledge-based approach for interpreting genome-wide expression profiles. Proc Natl Acad Sci U S A. 2005;102(43):15545-50.
46. Mootha VK, Lindgren CM, Eriksson KF, Subramanian A, Sihag S, Lehar J, et al. PGC-1alpha-responsive genes involved in oxidative phosphorylation are coordinately downregulated in human diabetes. Nat Genet. 2003;34(3):267-73.
47. Koopmans F, van Nierop P, Andres-Alonso M, Byrnes A, Cijsouw T, Coba MP, et al. SynGO: An Evidence-Based, Expert-Curated Knowledge Base for the Synapse. Neuron. 2019;103(2):217-34 e4.
48. McPherson CE, Eipper BA, Mains RE. Multiple novel isoforms of Trio are expressed in the developing rat brain. Gene. 2005;347(1):125-35.
49. Portales-Casamar E, Briancon-Marjollet A, Fromont S, Triboulet R, Debant A. Identification of novel neuronal isoforms of the Rho-GEF Trio. Biol Cell. 2006;98(3):183-93.
50. Oevel K, Hohensee S, Kumar A, Rosas-Brugada I, Bartolini F, Soykan T, et al. Rho GTPase signaling and mDia facilitate endocytosis via presynaptic actin. Elife. 2024;12.
51. Kaufmann WE, Moser HW. Dendritic anomalies in disorders associated with mental retardation. Cereb Cortex. 2000;10(10):981-91.
52. Huttenlocher PR. Dendritic development and mental defect. Neurology. 1970;20(4):381.
53. Huttenlocher PR. Dendritic development in neocortex of children with mental defect and infantile spasms. Neurology. 1974;24(3):203-10.
54. Huttenlocher PR. Dendritic and synaptic pathology in mental retardation. Pediatr Neurol. 1991;7(2):79-85.
55. Purpura DP. Dendritic spine "dysgenesis" and mental retardation. Science. 1974;186(4169):1126-8.
56. Purpura DP. Dendritic differentiation in human cerebral cortex: normal and aberrant developmental patterns. Adv Neurol. 1975;12:91-134.
57. Kulkarni VA, Firestein BL. The dendritic tree and brain disorders. Mol Cell Neurosci. 2012;50(1):10-20.
58. Yan Y, Eipper BA, Mains RE. Kalirin-9 and Kalirin-12 Play Essential Roles in Dendritic Outgrowth and Branching. Cereb Cortex. 2015;25(10):3487-501.
59. Banerjee S, Vernon S, Ruchti E, Limoni G, Jiao W, Asadzadeh J, et al. Trio preserves motor synapses and prolongs motor ability during aging. Cell Rep. 2024;43(6):114256.
60. Carroll LS, Owen MJ. Genetic overlap between autism, schizophrenia and bipolar disorder. Genome Med. 2009;1(10):102.

61. Purcell SM, Moran JL, Fromer M, Ruderfer D, Solovieff N, Roussos P, et al. A polygenic burden of rare disruptive mutations in schizophrenia. Nature. 2014;506(7487):185-90.
62. Satterstrom FK, Kosmicki JA, Wang JB, Breen MS, De Rubeis S, An JY, et al. Large-Scale Exome Sequencing Study Implicates Both Developmental and Functional Changes in the Neurobiology of Autism. Cell. 2020;180(3):568-+.
63. Genovese G, Fromer M, Stahl EA, Ruderfer DM, Chambert K, Landen M, et al. Increased burden of ultra-rare protein-altering variants among 4,877 individuals with schizophrenia. Nat Neurosci. 2016;19(11):1433-41.
64. Fromer M, Pocklington AJ, Kavanagh DH, Williams HJ, Dwyer S, Gormley P, et al. De novo mutations in schizophrenia implicate synaptic networks. Nature. 2014;506(7487):179-84.
65. De Rubeis S, He X, Goldberg AP, Poultney CS, Samocha K, Cicek AE, et al. Synaptic, transcriptional and chromatin genes disrupted in autism. Nature. 2014;515(7526):209-15.
66. Iossifov I, O'Roak BJ, Sanders SJ, Ronemus M, Krumm N, Levy D, et al. The contribution of de novo coding mutations to autism spectrum disorder. Nature. 2014;515(7526):216-21.
67. Pinto D, Delaby E, Merico D, Barbosa M, Merikangas A, Klei L, et al. Convergence of genes and cellular pathways dysregulated in autism spectrum disorders. Am J Hum Genet. 2014;94(5):677-94.
68. Kirov G, Pocklington AJ, Holmans P, Ivanov D, Ikeda M, Ruderfer D, et al. De novo CNV analysis implicates specific abnormalities of postsynaptic signalling complexes in the pathogenesis of schizophrenia. Mol Psychiatry. 2012;17(2):142-53.
69. Schultz-Rogers L, Muthusamy K, Pinto EVF, Klee EW, Lanpher B. Novel loss-of-function variants in TRIO are associated with neurodevelopmental disorder: case report. BMC Med Genet. 2020;21(1):219.
70. Howes OD, Cummings C, Chapman GE, Shatalina E. Neuroimaging in schizophrenia: an overview of findings and their implications for synaptic changes. Neuropsychopharmacology. 2023;48(1):151-67.
71. Dabiri M, Dehghani Firouzabadi F, Yang K, Barker PB, Lee RR, Yousem DM. Neuroimaging in schizophrenia: A review article. Front Neurosci. 2022;16:1042814.
72. Harvey I, Ron MA, Du Boulay G, Wicks D, Lewis SW, Murray RM. Reduction of cortical volume in schizophrenia on magnetic resonance imaging. Psychol Med. 1993;23(3):591-604.
73. Suddath RL, Casanova MF, Goldberg TE, Daniel DG, Kelsoe JR, Jr., Weinberger DR. Temporal lobe pathology in schizophrenia: a quantitative magnetic resonance imaging study. Am J Psychiatry. 1989;146(4):464-72.
74. Zipursky RB, Lim KO, Sullivan EV, Brown BW, Pfefferbaum A. Widespread cerebral gray matter volume deficits in schizophrenia. Arch Gen Psychiatry. 1992;49(3):195-205.
75. Kowluru A. Friendly, and not so friendly, roles of Rac1 in islet beta-cell function: lessons learnt from pharmacological and molecular biological approaches. Biochem Pharmacol. 2011;81(8):965-75.
76. Kowluru A. Multiple Guanine Nucleotide Exchange Factors Mediate Glucose-Induced Rac1 Activation and Insulin Secretion: Is It Precise Regulatory Control or a Case of Two Peas from the Same Pod? ACS Pharmacol Transl Sci. 2021;4(5):1702-4.
77. Zhou S, Yu D, Ning S, Zhang H, Jiang L, He L, et al. Augmented Rac1 Expression and Activity are Associated with Oxidative Stress and Decline of beta Cell Function in Obesity. Cell Physiol Biochem. 2015;35(6):2135-48.
78. Veluthakal R, Thurmond DC. Emerging Roles of Small GTPases in Islet beta-Cell Function. Cells. 2021;10(6).
79. Asahara S, Shibutani Y, Teruyama K, Inoue HY, Kawada Y, Etoh H, et al. Ras-related C3 botulinum toxin substrate 1 (RAC1) regulates glucose-stimulated insulin secretion via modulation of F-actin. Diabetologia. 2013;56(5):1088-97.

80. Sylow L, Nielsen IL, Kleinert M, Moller LL, Ploug T, Schjerling P, et al. Rac1 governs exercise-stimulated glucose uptake in skeletal muscle through regulation of GLUT4 translocation in mice. J Physiol. 2016;594(17):4997-5008.
81. Ba W, van der Raadt J, Nadif Kasri N. Rho GTPase signaling at the synapse: implications for intellectual disability. Exp Cell Res. 2013;319(15):2368-74.
82. Broadbelt K, Byne W, Jones LB. Evidence for a decrease in basilar dendrites of pyramidal cells in schizophrenic medial prefrontal cortex. Schizophr Res. 2002;58(1):75-81.
83. Black JE, Kodish IM, Grossman AW, Klintsova AY, Orlovskaya D, Vostrikov V, et al. Pathology of layer V pyramidal neurons in the prefrontal cortex of patients with schizophrenia. Am J Psychiatry. 2004;161(4):742-4.
84. Ramaswamy S, Markram H. Anatomy and physiology of the thick-tufted layer 5 pyramidal neuron. Front Cell Neurosci. 2015;9:233.
85. Chen L, Melendez J, Campbell K, Kuan CY, Zheng Y. Rac1 deficiency in the forebrain results in neural progenitor reduction and microcephaly. Dev Biol. 2009;325(1):162-70.
86. Reijnders MRF, Ansor NM, Kousi M, Yue WW, Tan PL, Clarkson K, et al. RAC1 Missense Mutations in Developmental Disorders with Diverse Phenotypes. Am J Hum Genet. 2017;101(3):466-77.
87. Tahirovic S, Hellal F, Neukirchen D, Hindges R, Garvalov BK, Flynn KC, et al. Rac1 regulates neuronal polarization through the WAVE complex. J Neurosci. 2010;30(20):6930-43.
88. Pennucci R, Gucciardi I, de Curtis I. Rac1 and Rac3 GTPases differently influence the morphological maturation of dendritic spines in hippocampal neurons. PLoS One. 2019;14(8):e0220496.
89. Wiens KM, Lin H, Liao D. Rac1 induces the clustering of AMPA receptors during spinogenesis. J Neurosci. 2005;25(46):10627-36.
90. Ba W, Nadif Kasri N. RhoGTPases at the synapse: An embarrassment of choice. Small GTPases. 2017;8(2):106-13.
91. Pertz O. Spatio-temporal Rho GTPase signaling - where are we now? J Cell Sci. 2010;123(Pt 11):1841-50.
92. Bellanger JM, Astier C, Sardet C, Ohta Y, Stossel TP, Debant A. The Rac1- and RhoG-specific GEF domain of Trio targets filamin to remodel cytoskeletal actin. Nat Cell Biol. 2000;2(12):888-92.
93. Scala M, Nishikawa M, Nagata KI, Striano P. Pathophysiological Mechanisms in Neurodevelopmental Disorders Caused by Rac GTPases Dysregulation: What's behind Neuro-RACopathies. Cells. 2021;10(12).
94. Hajdo-Milasinovic A, Ellenbroek SI, van Es S, van der Vaart B, Collard JG. Rac1 and Rac3 have opposing functions in cell adhesion and differentiation of neuronal cells. J Cell Sci. 2007;120(Pt 4):555-66.
95. Corbetta S, Gualdoni S, Ciceri G, Monari M, Zuccaro E, Tybulewicz VL, et al. Essential role of Rac1 and Rac3 GTPases in neuronal development. FASEB J. 2009;23(5):1347-57.
96. Cui D, Jiang X, Chen M, Sheng H, Shao D, Yang L, et al. Activation of Rac1 Has an Opposing Effect on Induction and Maintenance of Long-Term Potentiation in Hippocampus by Acting on Different Kinases. Front Mol Neurosci. 2021;14:720371.
97. Herring BE, Nicoll RA. Long-Term Potentiation: From CaMKII to AMPA Receptor Trafficking. Annu Rev Physiol. 2016;78:351-65.
98. Duman JG, Blanco FA, Cronkite CA, Ru Q, Erikson KC, Mulherkar S, et al. Rac-maninoff and Rho-vel: The symphony of Rho-GTPase signaling at excitatory synapses. Small GTPases. 2022;13(1):14-47.
99. Ferraro F, Ma XM, Sobota JA, Eipper BA, Mains RE. Kalirin/Trio Rho guanine nucleotide exchange factors regulate a novel step in secretory granule maturation. Mol Biol Cell. 2007;18(12):4813-25.

100. Hong-Geller E, Cerione RA. Cdc42 and Rac stimulate exocytosis of secretory granules by activating the IP(3)/calcium pathway in RBL-2H3 mast cells. J Cell Biol. 2000;148(3):481-94.
101. Lecuona E, Ridge K, Pesce L, Batlle D, Sznajder JI. The GTP-binding protein RhoA mediates Na,K-ATPase exocytosis in alveolar epithelial cells. Mol Biol Cell. 2003;14(9):3888-97.
102. Momboisse F, Lonchamp E, Calco V, Ceridono M, Vitale N, Bader MF, et al. betaPIX-activated Rac1 stimulates the activation of phospholipase D, which is associated with exocytosis in neuroendocrine cells. J Cell Sci. 2009;122(Pt 6):798-806.
103. Pathak R, Delorme-Walker VD, Howell MC, Anselmo AN, White MA, Bokoch GM, et al. The microtubule-associated Rho activating factor GEF-H1 interacts with exocyst complex to regulate vesicle traffic. Dev Cell. 2012;23(2):397-411.
104. Doussau F, Gasman S, Humeau Y, Vitiello F, Popoff M, Boquet P, et al. A Rho-related GTPase is involved in Ca(2+)-dependent neurotransmitter exocytosis. The Journal of biological chemistry. 2000;275(11):7764-70.
105. Andreae LC, Burrone J. Spontaneous Neurotransmitter Release Shapes Dendritic Arbors via Long-Range Activation of NMDA Receptors. Cell Rep. 2015;10(6):873-82.
106. Lu HW, Trussell LO. Spontaneous Activity Defines Effective Convergence Ratios in an Inhibitory Circuit. J Neurosci. 2016;36(11):3268-80.
107. Haeussler M, Schonig K, Eckert H, Eschstruth A, Mianne J, Renaud JB, et al. Evaluation of off-target and on-target scoring algorithms and integration into the guide RNA selection tool CRISPOR. Genome Biol. 2016;17(1):148.
108. Chen S, Lee B, Lee AY, Modzelewski AJ, He L. Highly Efficient Mouse Genome Editing by CRISPR Ribonucleoprotein Electroporation of Zygotes. The Journal of biological chemistry. 2016;291(28):14457-67.
109. Nagy A. Manipulating the mouse embryo : a laboratory manual. 3rd ed. Cold Spring Harbor, N.Y.: Cold Spring Harbor Laboratory Press; 2003. x, 764 p. p.
110. Paul CA, Beltz B, Berger-Sweeney J. The nissl stain: a stain for cell bodies in brain sections. CSH Protoc. 2008;2008:pdb prot4805.
111. Franklin KBJ, Paxinos G. Paxinos and Franklin's The mouse brain in stereotaxic coordinates. Fourth edition. ed. Amsterdam: Academic Press, an imprint of Elsevier; 2013. 1 volume (unpaged) p.
112. Feng G, Mellor RH, Bernstein M, Keller-Peck C, Nguyen QT, Wallace M, et al. Imaging neuronal subsets in transgenic mice expressing multiple spectral variants of GFP. Neuron. 2000;28(1):41-51.
113. Mertins P, Tang LC, Krug K, Clark DJ, Gritsenko MA, Chen L, et al. Reproducible workflow for multiplexed deep-scale proteome and phosphoproteome analysis of tumor tissues by liquid chromatography-mass spectrometry. Nat Protoc. 2018;13(7):1632-61.